OPTICAL SENSORS FOR MAPPING TEMPERATURE AND WINDS IN THE THERMOSPHERE FROM A CUBESAT PLATFORM

by

Stephanie Whalen Sullivan

A thesis submitted in partial fulfillment
of the requirements for the degree

of

MASTER OF SCIENCE

in

Electrical Engineering

Approved:

Dr. Charles Swenson Major Professor	Dr. Alan Marchant Committee Member
Dr. Todd Moon Committee Member	Dr. Mark R. McLellan Vice President for Research and Dean of the School of Graduate Studies

UTAH STATE UNIVERSITY
Logan, Utah

2013

Abstract

Optical Sensors for Mapping Temperature and Winds in the Thermosphere from a CubeSat Platform

by

Stephanie Whalen Sullivan, Master of Science

Utah State University, 2013

Major Professor: Dr. Charles Swenson
Department: Electrical and Computer Engineering

The thermosphere is the region between approximately 80 km and 320 or more km above the earth's surface. While many people consider this elevation to be "space" rather than atmosphere, there is a small quantity of gasses in this region. The behavior of these gasses influences the orbits of satellites, including the International Space Station, causes space weather events, and influences the weather closer to the surface of the earth. Due to the location and characteristics of the thermosphere, even basic properties such as temperature are very difficult to measure.

High spatial and temporal resolution data on temperatures and winds in the thermosphere are needed by both the space weather and earth climate modeling communities. To address this need, Space Dynamics Laboratory (SDL) started the Profiling Oxygen Emissions of the Thermosphere (POET) program. POET consists of a series of sensors designed to fly on sounding rockets, CubeSats, or larger platforms, such as IridiumNEXT SensorPODS. While each sensor design is different, they all use characteristics of oxygen optical emissions to measure space weather properties.

The POET program builds upon the work of the RAIDS, Odin, and UARS programs. Our intention is to dramatically reduce the costs of building, launching, and operating

spectrometers in space, thus allowing for more sensors to be in operation. Continuous long-term data from multiple sensors is necessary to understand the underlying physics required to accurately model and predict weather in the thermosphere.

While previous spectrometers have been built to measure winds and temperatures in the thermosphere, they have all been large and expensive. The POET sensors use new focal plane technology and optical designs to overcome these obstacles. This thesis focuses on the testing and calibration of the two POET sensors: the Oxygen Profiling of the Atmospheric Limb (OPAL) temperature sensor and the Split-field Etalon Doppler Imager (SEDI) wind sensor.

(85 pages)

Public Abstract

Optical Sensors for Mapping Temperature and Winds in the Thermosphere from a CubeSat Platform

by

Stephanie Whalen Sullivan, Master of Science

Utah State University, 2013

Major Professor: Dr. Charles Swenson
Department: Electrical and Computer Engineering

In the same way that mariners desire to know the weather their ships are about to encounter, satellite owners would like to know the conditions along their satellites' orbits. Accurate forecasts would allow operators to secure sensitive components prior to passing through a storm to reduce the risk of damage. Large solar arrays, which can act like sails, can be re-oriented to prevent the satellite from being moved out of its desired orbit. While terrestrial weather forecasters have thousands of sensors with continuous data streams available to generate weather models, very few sensors exist for space weather. Cost of sensing systems has been a major barrier for the space weather community. This thesis presents two sensors to measure weather in the thermosphere that can be produced and operated at a cost an order of magnitude lower than current systems.

High spatial and temporal resolution data on temperatures and winds in the thermosphere are needed by both the space weather and earth climate modeling communities. To address this need, Space Dynamics Laboratory (SDL) started the Profiling Oxygen Emissions of the Thermosphere (POET) program, which is the focus of this thesis. POET

consists of a series of sensors designed to fly on sounding rockets, CubeSats, or larger platforms, such as IridiumNEXT SensorPODS. While each sensor design is different, they all use characteristics of oxygen optical emissions to measure space weather properties.

The POET program builds upon the work of the RAIDS, Odin, and UARS programs. Our intention is to dramatically reduce the costs of building, launching, and operating spectrometers in space, thus allowing for more sensors to be in operation. Continuous long-term data from multiple sensors is necessary to understand the underlying physics required to accurately model and predict weather in the thermosphere.

To my husband, for his love, patience, and support.

Acknowledgments

Most of the work in this thesis was funded by the Space Dynamics Laboratory (SDL) in Logan Utah. Many individuals at SDL were instrumental in this research. I would like to specifically thank Dr. Alan Marchant for his optical designs, Erik Stromberg and Steven Grover for their mechanical design and CAD models, and Jed Simmons for assistance with optical testing. I would also like to thank the Spring 2012 Utah State University Space Design Class for their work on designing the host spacecraft. Dr. Andy Christensen provided the model of oxygen emissions and data from the RAIDS mission and was a great help understanding the requirements of the scientific community.

Stephanie W. Sullivan

Contents

List of Tables

List of Figures

Chapter 1

Introduction

The thermosphere is the region in the atmosphere between the mesosphere and the exosphere. The lower boundary of the thermosphere is defined by the mesopause, which is a low temperature layer between 80 km and 90 km above the earth's surface. The upper boundary of the thermosphere is not well defined. Various sources cite the upper boundary of the thermosphere between 320 km and 1,000 km [1, 2]. Since the density of the atmosphere in the thermosphere exponentially decays with altitude, only the lower portion has a sufficient quantity of gasses to measure.

Much of the understanding of the thermosphere is based on models. These models are used to study the effects of geomagnetic storms as well as quiet time conditions. Since current thermosphere temperature and wind measurements are spatially sparse, most reports only discuss thermosphere changes with altitude, as shown in Figure 1.1 [3].

Current measurement techniques include ground, rocket, and spacecraft-based instruments. Ground instruments are the lowest cost instruments and are capable of long term measurements, but only at a single spatial point with coarse altitude resolution. Rocket-based instruments achieve better altitude resolution, but forego temporal duration. A low-cost form of satellite temperature measurements is to study changes of satellite orbits due to drag. These studies do not require any sensors on the satellite, only observations of the satellite orbit and an understanding of the satellite drag profile. This is a common method of measuring thermosphere temperature, but unfortunately the measurements only show orbit-average temperature. Fully instrumented spacecraft are capable of repeated temporal and spatial altitude-resolved measurements. While satellites produce excellent data sets, they are the most expensive instruments.

There are multiple satellite-based instrument concepts. In situ measurements, where a

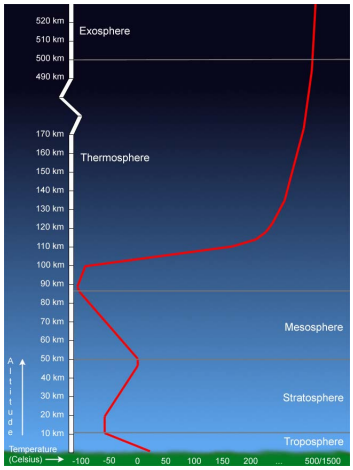

Fig. 1.1: Temperature in the upper atomsphere.

sensor on a satellite measures the atmosphere in the immediate area, are common. These are well understood, but are only capable of collecting data along the orbit of the satellite. Remote sensors are capable of covering a larger spatial area, often at multiple altitudes. Remote sensors for winds often measure Doppler shifts of known optical emission lines. Remote sensors for temperature can measure Doppler broadening of known emission lines or the behavior of a temperature-dependent spectrum. Doppler broadening of emission lines requires incredibly fine spectral resolution, which is rarely possible unless the instrument is also a Doppler wind sensor. Observing the behavior of spectra known to vary with temperature is the most promising temperature measurement technique.

1.1 Previous Work

The basic techniques for temperature and wind measurements have been demonstrated by multiple satellites. Oxygen in the thermosphere naturally emits light. Highly resolved spectral images of these emissions can be used to determine winds and temperatures at the location of the emission.

1.1.1 How to Obtain Temperature from Oxygen Emissions

The diatomic oxygen atmospheric band (A-band) consists of two major peaks near 762 nm. This emission line is caused by diatomic oxygen molecules being excited by sunlight.

The temperature dependence of the A-band emissions is well understood [4–6]. As the temperature increases, the relative intensity of the lower wavelength peak remains nearly constant while the upper wavelength peak drops. While many molecular spectra change with temperature, the dual-peak A-band is unique in that the relative intensity changes, not just the absolute intensity. This fact allows for accurate measurements to be made by a sensor with only relative spectral calibration. Absolute radiometric calibration is not necessary. Sensors that need only relative calibrations can be made much smaller and cheaper than sensors requiring absolute radiometric calibrations.

A detailed model of the O2 A-band temperature dependency has been developed by Andy Christensen based on work by Hertzberg. The Christensen model outputs theoretical emission spectra at temperatures from 150 to 1500 K on 3 degree increments at the wavelengths of the RAIDS/NIRS instrument [7]. A simulated emission spectra for selected temperatures from Christensen's model is shown in Figure 1.2. A best-fit match between model data and observed data is used to determine temperature. This technique has been demonstrated on the RAIDS and OSIRIS sensors [4, 5].

1.1.2 How to Obtain Wind Measurements from Oxygen Emissions

Doppler measurements are a common method of remotely measuring wind speeds. In an active system, a source emits an electromagnetic wave at a known wavelength. This wave travels to an object, scatters off, and returns to a detector as shown in Figure 1.3. If the object is stationary, the returning wave is at the same frequency as the sending wave. If the object is moving, the backscattered frequency is higher or lower, depending on the direction of motion. Since the wave travels at the speed of light and the motion of the object is much slower, the shift in frequency is very small.

Since the signal received by the detector is proportional to area of target molecules divided by the distance squared, a very large laser or radar source would be required for active measurements in the thermosphere. A passive Doppler system senses light emitted by the molecules of interest (shown in Figure 1.4) rather than light scattered off the molecules (as shown in Figure 1.3). The wavelengths of emissions in the thermosphere are well de-

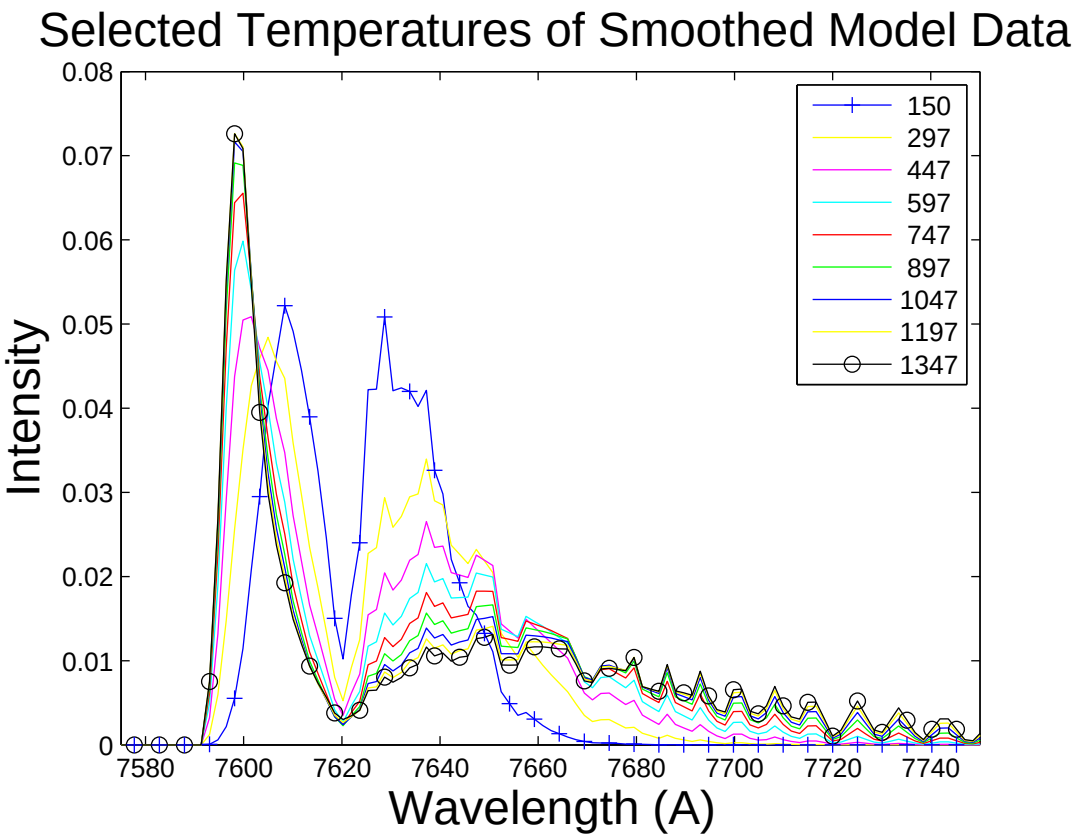

Fig. 1.2: Intensity of O2 A-band emissions shown for multiple temperatures at predicted resolution of the OPAL sensor.

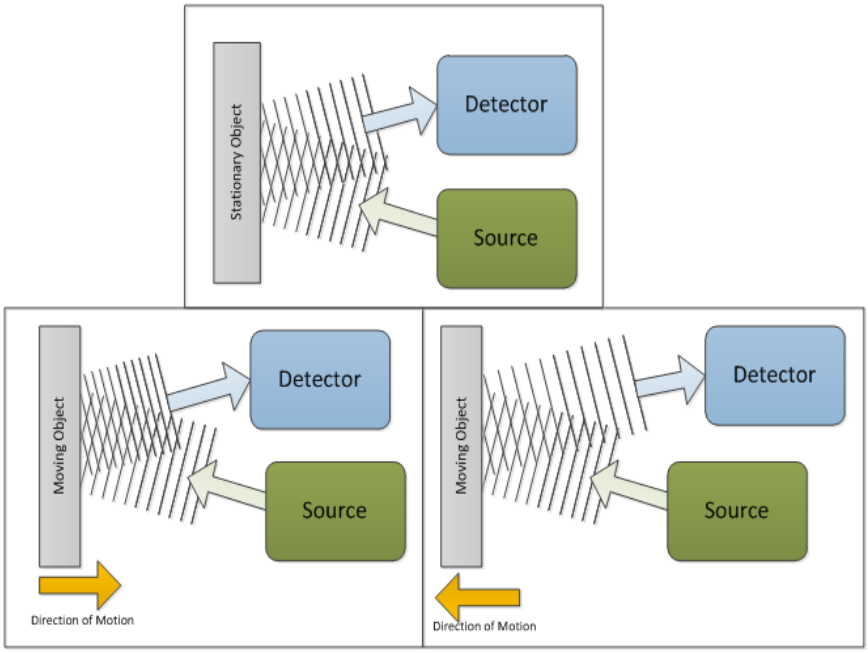

Fig. 1.3: Change in active Doppler signal frequency due to reflection off moving object.

scribed in the literature. No laser or radar source is required. The detector and processing are similar. Since the light does not bounce off the moving particles, the observed Doppler shift from a passive system is half that of an active system. Passive Doppler systems are preferred for thermosphere measurements due to the simplicity of the systems.

Doppler measurements only produce one-dimensional wind measurements along the line of sight of the instrument. By taking images from two different locations simultaneously, the two measurements can be combined to produce a two-dimensional wind vector. Figure

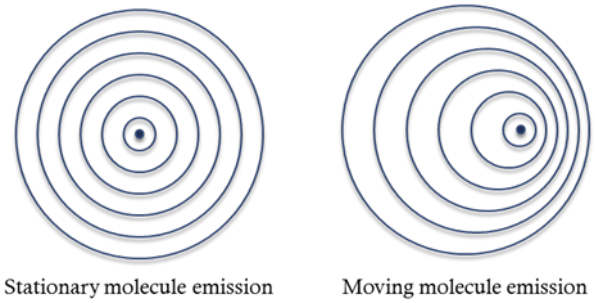

Fig. 1.4: Passive Doppler shift.

1.5 shows the forward and aft measurements made by a single instrument. Since a satellite moves very quickly relative to the atmosphere, measurements at two locations taken by the same satellite are approximately simultaneous, thus only one satellite is necessary to make both measurements.

Doppler measurements to determine wind speeds are based on very simple principles. The difficulty associated with these instruments is that the wavelength shift is very small. Typical spectrometers measure wavelength at the nanometer level. To detect wind speed, the sensor must detect at the picometer level. While picometer sensitivities are not uncommon, they typically require large, delicate instruments that are not suitable for spaceflight.

1.2 Previous Satellites

Previous space-based thermospheric profiling has produced high quality short temporal data which has been adequate to provide reasonable modeling bases. While these sensors have been excellent trailblazers, they have been resource-intensive, requiring costly platforms to operate. POET will build upon the legacy and theory of these sensors on a lower cost platform. This will make feasible the continuous long-term data collection required for accurate modeling.

1.2.1 WINDII and HRDI on UARS

The Upper Atmosphere Research Satellite (UARS) containing multiple sensors launched in September 1991. The WIND Imaging Interferometer (WINDII) measured wind, temperature and emission rates from 80-300 km altitudes. WINDII used a Michelson interferometer to detect Doppler shifts of multiple emission lines [8]. The High-Resolution Doppler Imager (HRDI) was a Fabry-Perot spectrometer to measure Doppler shifts of absorption lines to determine wind speeds in the lower thermosphere and lower regions [9]. Both instruments produced high quality data and operated for many years. HRDI finished its mission in 2005 [10]. The UARS satellite was deactivated in 2005 and deorbited in September 2011. UARS is shown to scale with a silhouette of a 6-foot person in Figure 1.6 [11].

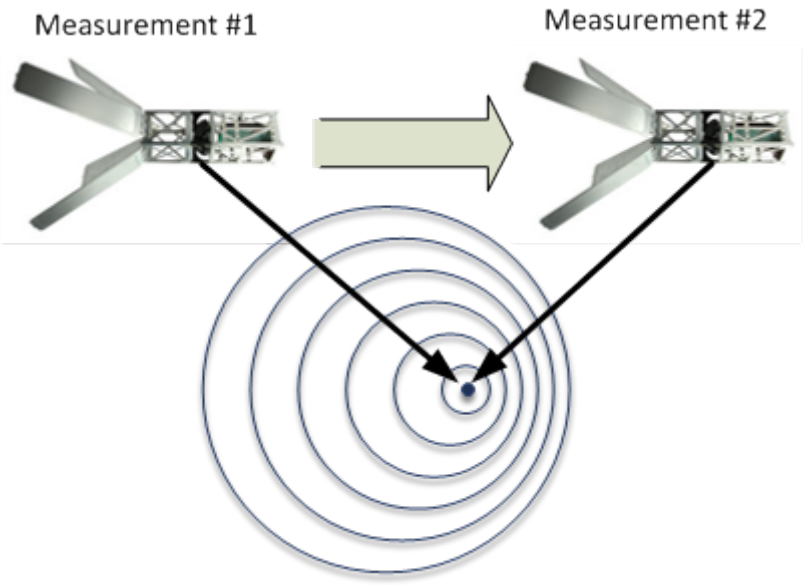

Fig. 1.5: Configuration for two-dimensional wind measurements. Satellite takes an image of the area of interest, moves forward, and takes a second image of the same area of interest.

Fig. 1.6: The UARS satellite shown with a scaled image of a 6 foot tall person.

1.2.2 OSIRIS on Odin

The Optical Spectrograph and InfraRed Imaging System (OSIRIS), shown in Figure 1.7 [12], was launched on the Odin satellite in February 2001. OSIRIS measures the atomic A-band at a resolution of 0.4 nm and the entire band of 275-810 nm at 1 nm resolution. Temperatures were determined for the 90-110 km altitude range by fitting the A-band observations to modeled data with accuracies of +/-2 Kelvin at 90 km [4].

1.2.3 TIDI and SABER on TIMED

The Sounding of the Atmosphere using Broadband Emission Radiometry (SABER) instrument was launched on the Thermosphere Ionosphere Mesosphere Energetics and Dynamics (TIMED) satellite in 2001. It is a large instrument that is capable of measuring the temperature of the thermosphere from emission spectra, as well as other properties of the thermosphere. The SABER instrument alone is 65.6kg [13] and requires a very large satellite platform, as shown in Figure 1.8 [13].

The TIMED Doppler Interferometer (TIDI), which operated from 2002-2005, was another sensor on the TIMED satellite [14]. TIDI used multiple telescopes with a Fabry-Perot interferometer to measure winds and temperatures in the mesosphere and lower thermosphere/ionosphere region. TIDI measured winds with approximately 2 km vertical resolution and 3 m/s accuracy [15].

1.2.4 RAIDS on the International Space Station

The Remote Atmospheric and Ionospheric Detection System (RAIDS) operated from the Kibo module of the International Space Station (ISS) from October 2009 through December 2010. It measured a variety of emission spectra from 80-180 km altitudes. RAIDS studied the photochemical reactions of oxygen observable in the thermosphere. A model for Atmospheric Band limb brightness was developed and tested against observed data. The temperature dependent spectra from this model were used to estimate temperature from the observed emission spectra [7]. The RAIDS instrument is shown in its operational location in Figure 1.9 [16].

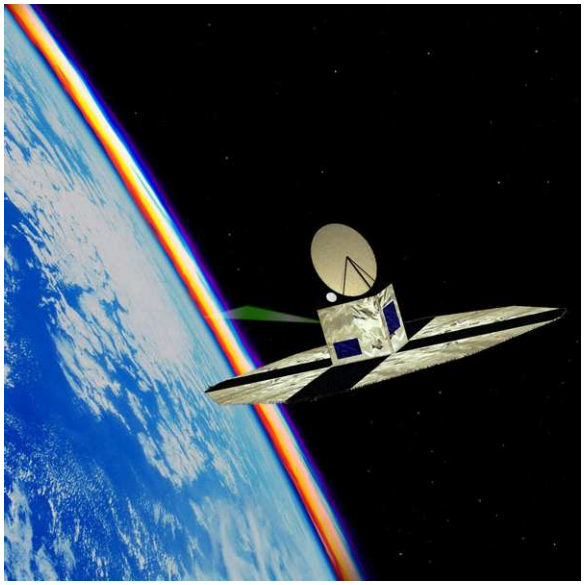

Fig. 1.7: ODIN Satellite.

Fig. 1.8: SABER Satellite.

Fig. 1.9: RAIDS (gold object in white housing) mounted on the International Space Station.

1.2.5 CubeSats

Most satellites are fully custom designs. This is common because each satellite has unique requirements and no space or power available for unnecessary items. Unfortunately, this design practice makes satellites incredibly expensive. CubeSat is a standard satellite design created by California Polytechnic State University with Stanford University and is well accepted within the small satellite community. Basic dimensions, weight, and safety requirements are defined. CubeSats are defined by how many 10 cm cubes make up the satellite. 1-U (10 x 10 x 10 cm), shown in Figure 1.10 [17], and 3-U (30 x 10 x 10 cm) are common sizes. These standards allows for use of a common launcher, the Poly-Pico Satellite Orbital Deployer (PPOD), to be used for all CubeSats to interface with the launch vehicles. Due to the standardization of safety requirements and launch vehicle integration procedures, as well as encouragement by NASA, many launch providers will allow PPODS to fill excess space on a launch vehicle, resulting in launch costs of tens of thousands of dollars for a CubeSat compared to tens of millions of dollars for the primary satellite.

The CubeSat standard has also encouraged development of standardized hardware that can be purchased as commercial-off-the-shelf (COTS) items rather than developed custom for each satellite. Attitude determination sensors, attitude, and position control actuators, solar panels, power conditioning electronics, radios, and other hardware are available as COTS items. SDL has developed a high capability avionics stack for a CubeSat form factor. The reusability of parts across multiple satellites has dramatically reduced the cost

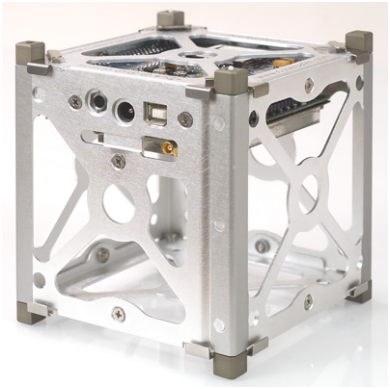

Fig. 1.10: 1-U CubeSat.

and schedule of designing and building CubeSats.

The cost of building, launching and operating a CubeSat is a small fraction of historical satellite costs. While many of the cost savings relate to standardization, part of the cost savings is due to the small size of the satellite, which has some draw backs, such as reduced power production capability. Initially, it was thought that these limitations would only allow academic satellite missions to use the CubeSat platform. However, due to the miniaturization and enhanced capability of processors, sensors, and other electronics, it is now feasible to conduct experiments of scientific value from a CubeSat. The dramatically lowered cost makes multiple satellites for simultaneous measurements feasible.

1.3 Thesis Objectives

The objectives for this thesis were to design sensors based on the principles demonstrated by previous satellites, but in a form factor compatible with a CubeSat host vehicle. This will allow for excellent science at a reasonable price.

This thesis focuses on two sensors, the OPAL temperature sensor and the SEDI wind sensor. As part of this thesis: OPAL was built and tested, SEDI was designed and a test plan developed, and preliminary designs for both mission concepts and host spacecraft were completed. SEDI testing should be complete in late 2012, but will not be addressed in this thesis.

Chapter 2

POET Sensors

The Profiling Oxygen Emissions of the Thermosphere (POET) program consists of two sensors. The first sensor is the Oxygen Profiling of the Atmospheric Limb (OPAL) sensor, which measures emission lines to determine temperature. The second sensor is the Split-field Etalon Doppler Imager (SEDI) sensor, which measures the Doppler shift of emission lines to determine wind velocity.

2.1 Oxygen Profiling of the Atmospheric Limb (OPAL)

The OPAL instrument is a high resolution imaging spectrometer that simultaneously collects spatially-resolved A-band spectra in multiple azimuthal directions and across the full altitude range of A-band emission. The spectral data can be converted to temperature at each spatial point. OPAL is based on the analysis techniques described in Section 1.1.1. OPAL has size, weight, and power compatible with a 3-U CubeSat platform.

2.1.1 Limb Viewing

The atmospheric limb is the view of the atmosphere seen when looking along a line tangent to the altitude of interest, as shown in Figure 2.1. A tangent view is ideal for studying gasses in the thermosphere because of the incredibly sparse density. The tangent view looks through a larger volume at the altitude range of interest than an up or down-looking sensor. The additional signal levels from a limb viewing condition allow OPAL to measure finer spatial resolutions than other viewing configurations. The tangent view includes signal components from all the altitudes between the altitude of interest to the altitude of the sensor. Since OPAL simultaneously collects data at many altitudes, the data can be deconvolved to determine the apparent temperature profile.

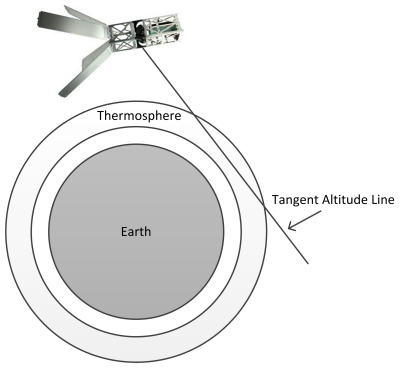

Fig. 2.1: Satellite observing the atmospheric limb along a tangent line.

2.1.2 Spatial Data Collection

While previous instruments have only measured one spatial data point at a time, OPAL collects many simultaneously. OPAL takes vertical line samples at nine horizontal locations, as shown in Figure 2.2. Horizontal spacing between consecutive locations is approximately 50 km. Each vertical sample is dispersed, as shown in Figure 2.3, to measure the spectral content of each pixel in the sample. The vertical information of each sample is preserved with a resolution of approximately 5 km. Horizontal information is obtained by collecting multiple vertical line samples. All data is collected simultaneously on a single focal plane array. The location of pixels correlates to wavelength of light, so a monochromatic focal plane array (FPA) is used for the detector. Sample sets can be collected at approximately 20 second intervals, resulting in approximately 150 km spacing along the orbit. The expected performance metrics of the flight model OPAL are compared to the metrics required by the science community in Table 2.1. Most of the science community requirements were developed for the CUPID project in 2011 [18]. Field of view (FOV) is a minimum requirement and IFOV is a maximum requirement.

2.1.3 Optics

Light emitted by oxygen molecules in the thermosphere is imaged by the OPAL instrument. Light enters the deployed shade baffle on the nadir face of the satellite. Two angled mirrors direct the light into the OPAL optics box, which is shown in Figure 2.4.

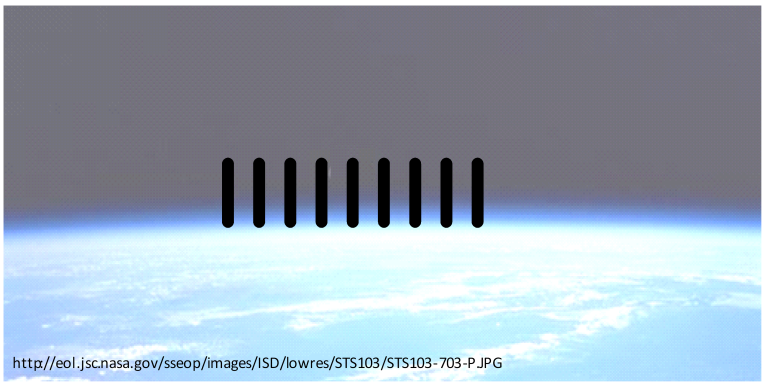

Fig. 2.2: OPAL collects samples along vertical lines.

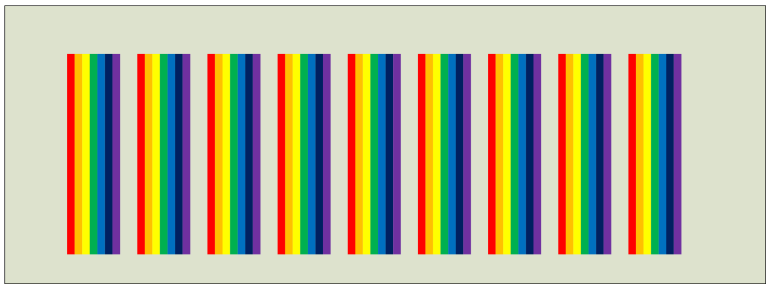

Fig. 2.3: Vertical lines are dispersed with a grating to show spectral components. If a broadband source was imaged, the focal plane would detect a rainbow-like spectrum for each slit.

Table 2.1: OPAL spatial resolution.

Dimension	Required	Expected	Units	Requirement Source
Along-track IFOV	280 max	150	km	CUPID Proposal
Cross-track IFOV	280 max	45	km	CUPID Proposal
Cross-track FOV	300 min	400	km	Author
Vertical IFOV	5 max	0.85	km	CUPID Proposal
Vertical FOV	50 min	85	km	CUPID Proposal

The OPAL optics box consists of a small refractive telescope that focuses the scene onto a multi-slit array, with slits oriented in the vertical direction. An optical bandpass filter removes out-of-band light. A spectrometer reimages light from the slits onto a focal plane array (FPA) with a high degree of spectral dispersion in the direction perpendicular to the slits. The spectrometer section consists of a triplet collimating lens, a volume holographic grating (VHG) [19] and a reimaging triplet lens. The OPAL optical layout and CAD model are shown in Figure 2.4 left and right, respectively. These figures do not show the front fold mirror or the deployed shade baffle.

The OPAL entrance aperture is 5 mm tall (vertical direction) by 14 mm wide. This small aperture enhances the optical alignment tolerance while providing sufficient spatial resolution and light-gathering capability.

The three triplet lens groups are identical. This design principle lowers the cost of fabrication and simplifies the process of alignment. The bandpass filter is a custom interference filter consisting of a narrow-band transmission filter and a broadband blocking filter that attenuates out-of-band scene radiance by 10^{-4} across the sensitivity range of the focal plane.

2.1.4 Detector

The standard detector for the OPAL instrument is SDL's Digital Imaging Space Camera (DISC). Originally developed as a star camera, the detector is a compact, low-power, space qualified, low-noise device. Upgrading to an EMCCD detector by e2v Technologies would improve the signal to noise ratio, allowing for increased spatial sampling.

The focal plane array (FPA) in the DISC camera is a model HAS2 from On Semiconductor (formerly Cypress / Fill Factory). HAS2 is a radiation-hardened imager with 28% photon detection efficiency (quantum efficiency x fill factor) at 760 nm [20]. The device performs all image readout functions, including 12-bit digitization. The HAS2 has relatively low read noise. However, dark current is a concern at the low-light levels of limb imaging. In order to achieve sufficiently low dark current, the FPA will be cooled by a thermoelectric cooler to an operating temperature of -15 degrees Celsius. The DISC controller manages

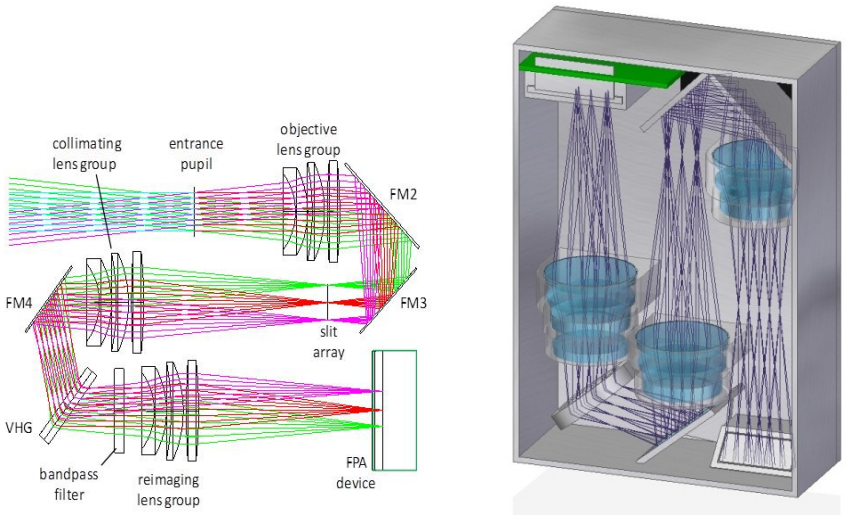

Fig. 2.4: OPAL optics. Left: Detailed elements with ray trace. Right: Optics shown to scale in CubeSat payload bay.

operation of the FPA and thermal controls (TE cooler and trim heater) and collects and formats the stream of hyperspectral images and metadata from OPAL.

2.1.5 Stray Light Control

The OPAL instrument must deal with a wide range of radiance levels within and near the limb scene. A-band radiance at 90 km is at least 20 times greater than at 140 km. The limb brightness may be even greater at lower elevations. Clouds are a thousand times brighter and can be found just 3 degrees below the center of the FOV. Therefore it is essential that OPAL have strong rejection of near-scene illumination and low levels of in-scene scattering. A shade assembly positions the entrance aperture 200 mm from the entrance pupil. This 14 x 54 mm aperture blocks stray light from scene sources that are more than 1.4 degrees below the center of the FOV. As illustrated in Figure 2.5, the shade assembly extends beyond the nominal spacecraft envelope. It is a spring-loaded pop-up structure that collapses to fit within the PPOD envelope, then deploys on orbit. The deployed mirror is also spring-loaded and deploys along with the shade assembly.

The dominant source of stray light within OPAL will be the bright lower edge of the

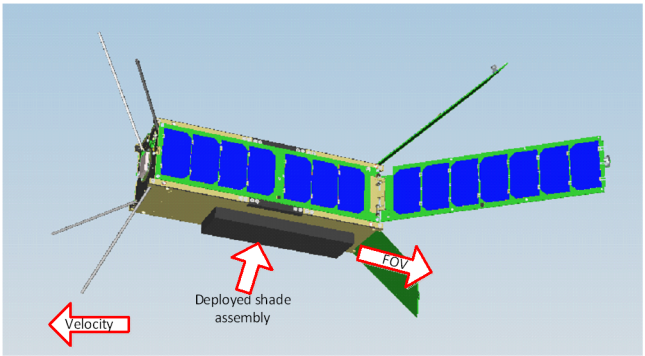

Fig. 2.5: Deployed shade baffle on OPAL host spacecraft.

earth's limb immediately below the desired field of view. The OPAL entrance aperture provides less stray light rejection in the horizontal direction, consistent with the structure of the limb scene. Solar or lunar illumination of the entrance aperture only occurs when the sun or moon is viewed through the limb of the earth. In these rare situations, no data will be collected.

Veiling glare occurs when a small fraction of light from a very bright source is scattered within the instrument. This happens due to minor imperfections in the optics and cannot be completely eliminated. Veiling glare prevents measurements of very bright and very dim sources in the same image. Small-angle scattering creates veiling glare that competes with the signal from dimmer regions of the limb scene. Veiling glare cannot be compensated as easily as the spectrally diffuse background because light from the lower limb has a negative, self-absorbed A-band signature. The primary source of veiling glare will be the first two mirrors in the optics train. All of the OPAL mirrors will be specified with high-quality surface finish. Preliminary analysis indicates that this will hold stray light below 1% at the top of the limb scene. Secondary and higher-order stray light will be mitigated by use of diffuse black paint on internal surfaces of the shade assembly, telescope, and spectrometer.

2.1.6 Thermal Subsystem

OPAL is designed to operate within the temperature range of -30 to +40 degrees Celsius, with survival temperatures covering -50 to +85 degrees Celsius. These temperatures

are consistent with a CubeSat in a high inclination low earth orbit. The OPAL instrument is divided into two main temperature zones: 1) optical housing/electronics, and 2) FPA. All of the components within the first zone are thermally tied to the aluminum containment structure, which mounts to the CubeSat. Heaters will be provided in this section to prevent ice from forming on the optics. The second temperature zone supports the FPA, which will be cooled to -15 degrees Celsius. The second zone will be thermally isolated and will contain a thermoelectric cooler.

2.1.7 Electrical Subsystem

The only electric components in OPAL are the heater, thermoelectric cooler, and detector. The OPAL detector has two electronics boards that interface directly with the CubeSat bus. The default size of the boards is 9.5 x 9.5 x 2 cm, but the shape of these boards can be modified to fit in the space available on the CubeSat. The DISC electronics operate the FPA, command the temperature controls, and window the OPAL data. Additional processing capability will be provided by a daughter board. Since information of potential value may be lost in the data compression process, only the minimum processing required to meet downlink capabilities will be performed. Data processing includes image calibration, formatting, and data compression. Image calibrations apply pixel-wise corrections for the known characteristics of pixel operability, dark offset, and pixel gain. Formatting provides options for uncompressed downlink of individual spectrometer images, and continuous downlink of compressed spectrometer data. Onboard compression includes the following steps: 1) detection of the limb region, clipping the out-of-scene regions associated with spacecraft pointing offsets; 2) co-addition of detector rows associated with spatial oversampling in altitude; 3) co-addition of detector columns associated with spectral oversampling; 4) co-addition of detector regions associated with spatial oversampling horizontally; and 5) additional compression if required by spacecraft downlink limitations. Using only the existing data processing capabilities of the DISC camera, 14 Kbps orbit average of data will be produced. Using very aggressive data compression, 97 bps orbit average will be produced for continuous daylight observation.

2.1.8 CubeSat Platform

OPAL is designed to fly on a 3-U CubeSat because this platform is relatively inexpensive, as discussed in Section 1.2.5. The ability to make cost effective sensors on affordable platforms is required for high-spatial, high-temporal measurements. OPAL has low size, weight, and power requirements. Other interface requirements, such as data downlink capacity, attitude control, and processing capability, are feasible on a well-designed CubeSat. These requirements are presented in Table 2.2.

2.1.9 OPAL Summary

OPAL is designed to collect meaningful scientific data. The spatial and temperature resolution are fine enough to study temperature variations induced by geomagnetic storms. It maximizes the use of existing techniques and flight hardware. The low cost of the OPAL system allows for a financially feasible constellation to measure both spatial and temporal changes in the thermosphere at a resolution never before possible. Characteristics of OPAL are listed in Table 2.3.

2.2 Split-field Etalon Doppler Imager (SEDI)

The SEDI instrument is a passive Doppler imager. It measures wind speeds in the thermosphere based on the theory discussed in Section 1.1.2. SEDI is unlike previous sensors because it is small enough to fit in a 6-U CubeSat. (The instrument is actually small enough to fit in a 2-U package, but the required supporting equipment pushes the preferred satellite size to 6-U.)

2.2.1 Measurement Technique

To measure two-dimensional wind velocity, two measurements of the same airmass must be obtained, as discussed in Section 1.1.2. Common methods of collecting multiple measurements are to use multiple sensors or to use a single sensor and rotate or move it around the airmass. SEDI uses a simplified method. Only a single satellite is used for cost reasons. Rather than maneuver the satellite, the sensor has forward and aft apertures. As

Table 2.2: OPAL instrument spacecraft interface requirements.

Requirement	**Value**	**Requirement**	**Value**
Mass	500 g Optics 200 g Electronics 70 g Baffle 770g Total	**Dimensions**	4 x 14 x 9.5 cm (not including external shade and electronics)
Attitude Control	0.5 deg (2σ) pointing 0.07 deg (2σ) attitude knowledge	**Data Downlink**	551 bps, orbit average w/ aggregation
Flight Orientation	maintain 10 deg pitch and 5 deg yaw	**Data Bus**	RS-422
Power	6 W, peak 4.35 W, orbit average	**Temperature Range**	-30 to +40C operating temperature range (not incl. FPA) -50 to +85C survival temperature range
Voltage	12VDC and 5VDC	**Thermal Control**	350mW TEC
External Shade Assembly	22 x 3 x 6.5 cm deployed on the nadir surface	**FPA Radiator**	anti-ram face

Table 2.3: OPAL instrument characteristics and design parameters.

Characteristic	**Description**	**Characteristic**	**Description**
Measurement Method	High Resolution Limb Spectroscopy	**Bandwidth**	758 - 770 nm
Instrument Type	Hyperspectral Imaging Spectrometer	**Field of View***	44 mrad, vertical 188 mrad, horizontal
Heritage	RAIDS (limb spectroscopy) DISC (CMOS FPA)	**Resolution***	0.5 nm, spectral 0.4 mrad, vertical 24 mrad, horizontal
TRL	5 (spectrometer) 7 (electronics)	**IFOV* (Sampling)**	0.16 nm (spectral) 0.32 mrad (vertical) 24 mrad (horizontal)
SNR	20 at 140 km 200 at 90 km	**Slit Array**	10.4 x 2.4 mm 9 slits, width 55 m
Optical Throughput	87% foreoptics 50% spectrometer	**Sample Period**	20 s
		Focal Length	55 mm, f:4
FPA Radiation Tolerance	200 krad	**Collection Aperture**	5 x 14 mm
FPA	1024 x 1024 CMOS imager	**FPA Operating Temp**	-15C
Pixel Pitch	18 m	**Dark Current**	30 e-/s per pixel
QE X Fill Factor	28%	**Read Noise**	18 e-
Pixel Capacity	82,000 e- (linear)	**Readout Rate**	5 MHz w/ 12-bit DAC
* Viewing the limb (120 km altitude) from a 400 km orbit, 1 mrad corresponds to 1.9 km.			

the satellite flies along, the apertures look to the side, forward 45 degrees and aft 45 degrees. The aft aperture views the same thermosphere volumes as the forward aperture, but a few minutes later, as shown in Figure 2.6. The satellite always points along the velocity vector. This technique allows for a single satellite, with no moving parts or maneuvering to collect two-dimensional wind vectors.

2.2.2 Wavelength

There are a limited number of wavelengths available for passive Doppler imaging because passive systems can only operate with light *emitted* by a molecule in the region of interest, not reflected sunlight. A table of wavelengths emitted by atoms and molecules in the thermosphere is available from Khomich [21]. High intensity in both quiet and aurora conditions is necessary for monitoring of the thermosphere. Infrared detectors are more resource-intensive than optical detectors, so wavelengths longer than 1 micron are not advisable. The altitude range of 200-300 km is most interesting from a science perspective, so the atomic oxygen line at 630.0 nm was selected for use in SEDI.

2.2.3 Detection Method

Measuring Doppler shifts to detect winds requires spectral resolution on the order of pico-meters. There are few instruments capable of this resolution. Michelson interferometers are standard detectors capable of this resolution. They are common in ground-based instruments, but due to the requirement for moving parts they are not desirable for space-based instruments. Spatial heterodyne techniques are being developed by NRL [22]. These techniques show promise, but require instruments too large for a CubeSat mission. Fabry-Perot interferometers are classic instruments for high spectral resolution measurements. They require no moving parts and are well understood. A Fabry-Perot interferometer was selected for SEDI.

2.2.4 Fabry-Perot Data

When light passes through a Fabry-Perot etalon it adds constructively if it is in-phase

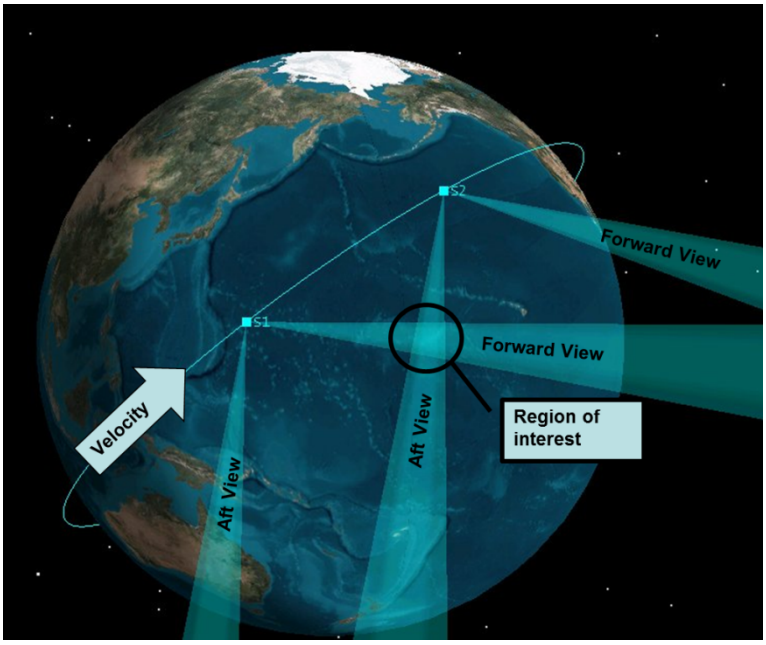

Fig. 2.6: Region of interest viewed twice by the same satellite.

or destructively if it is out of phase. Light being in-phase is dependent on the length of the etalon (l in Figure 2.7 below), the material of the etalon, and the wavelength and angle of incidence of the light. Fabry-Perot interferometers must be built for the frequency of interest. Narrow band-pass filters must be used with Fabry-Perot etalons to prevent neighboring atmospheric emission lines from passing through.

When a narrow beam of light is passed through a Fabry-Perot etalon and the output focused into an image, the result is a set of concentric rings. Typical applications of Fabry-Perot sensors detect the presence or intensity of the rings. For applications where very fine spectral resolution is necessary, the phase shift of the rings is detected. Figure 2.8 [23] shows a simulated output from the SEDI interferometer. The phase shift between the left half and right half of the image is due to the Doppler shift caused by motion of the spacecraft. The phase shift between the top and bottom of the image is caused by 200 m/s winds.

2.2.5 Optics

The unfolded optics train for the SEDI sensor is shown in Figure 2.9. Two input apertures are oriented 90 degrees apart. These will be mounted in the spacecraft such

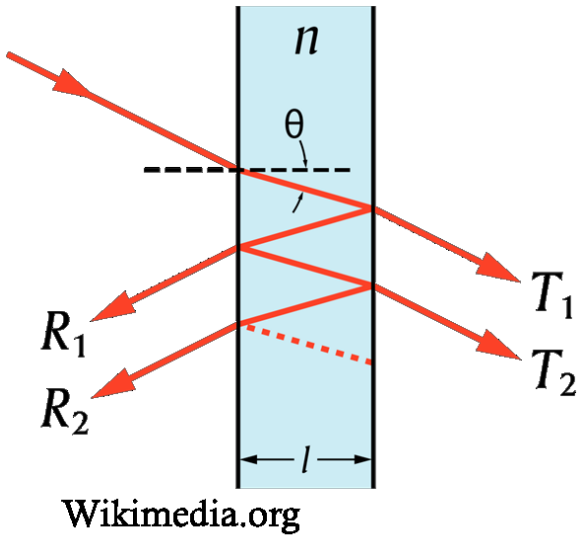

Fig. 2.7: Fabry-Perot interferometer.

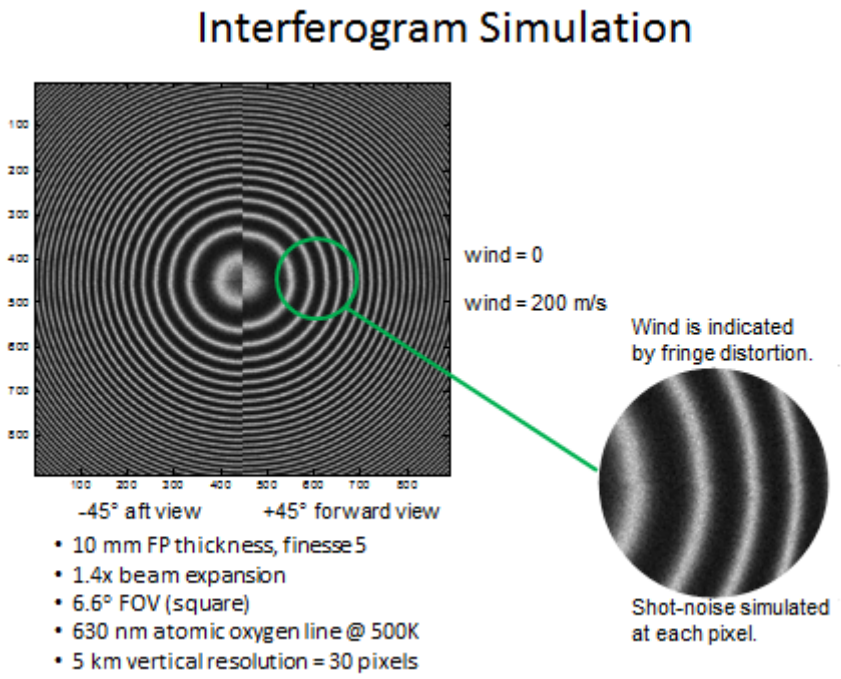

Fig. 2.8: Interferogram simulation.

that one is pointing 45 degrees forward and the other 45 degrees backward to collect data in accordance with the technique described in Section 2.2.1. To reduce the size of the sensor, both apertures share a common collimator, interferometer optics, and image sensor. This technique allows for only half of the field of view from each aperture to be preserved, resulting in only one horizontal measurement, but multiple vertical measurements for each data collection. This loss of horizontal data is appropriate because the horizontal field of view is smeared by the motion of the spacecraft while the vertical dimension is not.

The field sharing mirror located near the prime focus of both objective lenses sends half the light from each aperture into the instrument. A field stop blocks unwanted light. A 47 mm lens collimates the light into a single beam. A 2 nm bandpass filter removes most of the collected light. The Fabry-Perot filter passes only the 630.0 nm emission line of interest. A re-imaging lens focuses the collimated light onto a detector.

A neon lamp is used as a calibration source because it has a very stable emission line at 630.5 nm [24]. Since the neon lamp is inside the instrument, there will be no apparent Doppler shift. The phase shift between the limb interferogram and the neon interfereogram, combined with the knowledge of the neon emission line wavelength and spacecraft velocity will be used to determine the speed of particles in the thermosphere.

To fit the instrument described above into a CubeSat, the optics train must be folded multiple times. Figure 2.9 shows the folded optics train. The ray trace from the forward aperture is shown. The rays from the aft aperture (not shown) enter the instrument at a 90 degree angle to the light entering from the forward aperture. After the first fold mirrors, both light paths hit the aperture splitting mirror, after which point the light travels down the same path to the detector.

2.2.6 Detector

The thermosphere is not a bright source of light. With the SEDI sensor, only a very small fraction of incident light passes through the optics train. To obtain the necessary spatial resolution of the interferogram, only a few photons per second illuminate each pixel of the FPA. The two options for detectors in this instrument are a micro channel plate

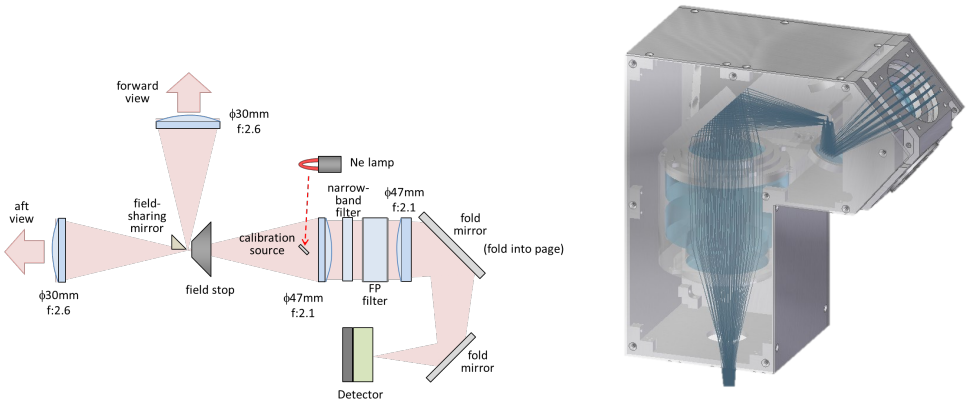

Fig. 2.9: SEDI Optics. Left image is unfolded. Right image shows optics to scale, folded into CubeSat form factor.

paired with a standard CMOS or CCD detector or an electron multiplying charge coupled device (EMCCD). The EMCCD is preferred due to greater sensitivity and reduced noise characteristics. The preferred device is CCD97-00 Back Illuminated 2-Phase Electron Multiplying CCD sensor by e2v Technologies, which is shown in Figure 2.10. A space rated electronics board for this sensor will be custom built by SDL.

2.3 Could SEDI Replace OPAL?

It is possible to determine temperature from Doppler broadening of known emission lines. Since SEDI has the sensitivity to measure Doppler shifts, it could also measure Doppler broadening. Unfortunately, the high spectral sensitivity of SEDI requires a large

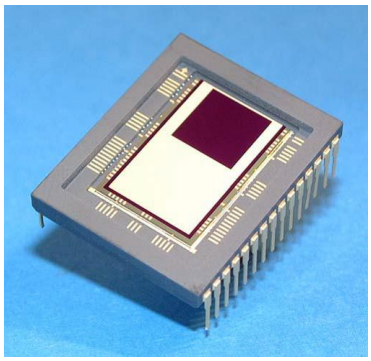

Fig. 2.10: Electron Multiplying Charge Coupled Device (EMCCD) by e2v Technologies.

input signal. To obtain a large input signal, the field of view or the exposure time must be increased. While both SEDI and OPAL can measure temperature in the thermosphere, OPAL has a much higher spatial resolution. Since SEDI and OPAL observe emissions from different gasses, OPAL operates at slightly lower altitudes than SEDI. SEDI could be used in the on-orbit calibration of OPAL, or to complement OPAL by extending the altitude range, but will not replace OPAL.

2.4 Alternate Packaging

The basic OPAL and SEDI sensors can be repackaged to fit mission requirements. The shape of the instruments can be changed by using different folding patterns for the optical elements of the sensor. The volume of the sensor is fairly constant, but the dimensions can change between a cube or a long rectangular volume. This allows OPAL or SEDI to be packaged with other instruments within the volume defined by the mission.

2.4.1 1-U OPAL

The optical layout of the 1-U OPAL folds the instrument into a cube rather than a long rectangle, as shown in Figure 2.11. Additional fold mirrors are added to achieve this compact configuration. The 1-U packaging can be used if this shape is more compatible with the host vehicle than the standard long rectangle.

2.4.2 STEADE

The Storm Time Energy & Dynamics Explorers (STEADE) program was proposed to NASA to be executed by Utah State University and Space Dynamics Laboratory. The objective of STEADE is to "understand how electromagnetic fields, energized by geomagnetic storms, deposit energy, heat and redistribute the Earth's charged and neutral atmosphere" [25]. A sensor suite is being developed to launch on satellites in the IridiumNEXT constellation to measure the data required to meet the objective. The OPAL sensor layout has been modified to fit next to an electric field sensor within the constraints of the SensorPODS, as shown in Figure 2.12.

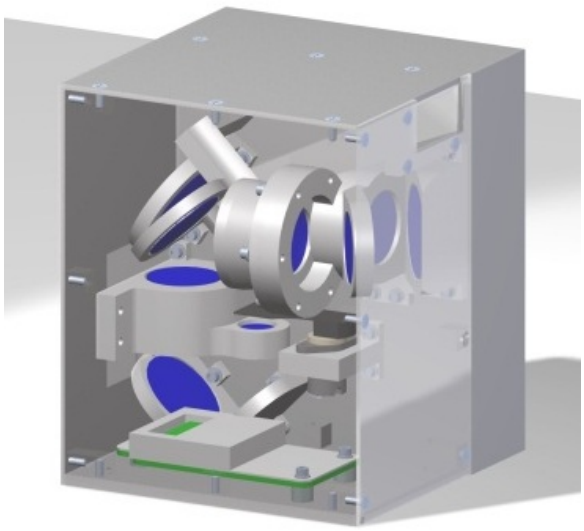

Fig. 2.11: OPAL optics and electronics in a 1-U volume.

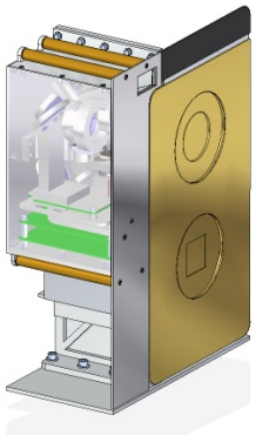

Fig. 2.12: OPAL in a SensorPODS configuration.

2.4.3 Rock-STEADE

The Rock-STEADE program is an adaptation of the STEADE sensor suite to operate from a sounding rocket rather than a satellite platform. It includes multiple instruments for measuring energy in the Aurora Borealis, including a POET temperature sensor. Rock-STEADE will be launched from Poker Flats, Alaska during an active aurora event to allow for in situ measurements of the geomagnetic storm. Rock-STEADE POET operates from the top of a rocket flying through the thermosphere. This allows for excellent horizontal resolution, as shown in Figure 2.13. Vertical resolution is calculated from upward looking data at multiple rocket positions and is limited only by the speed of data collection. While rockets can collect high resolution data, they are unable to repeat measurements at different locations or different times.

The Rock-STEADE instrument is different than other OPAL instruments because the science requirements only demand intensity in specific spectral bands. Rather than using a spectrometer, multiple bore-sighted photometers are used to characterize the spectral shape of the A-band.

2.4.4 2-U SEDI

SEDI can be packaged into a 2-U (20 x 10 x 10 cm) form factor. Unfortunately, the supporting hardware required for the SEDI sensor (electrical, attitude determination and control, data processing, communications, etc.) cannot currently fit into a 1-U package. Since the assembled satellite cannot fit into a 3-U, the smallest standard CubeSat size for SEDI is 6-U, which allows a 2-U volume for companion instruments. The wider SEDI layout presented above is more elegant than the 2-U layout. However, if a mission requires the 2-U form factor, it is possible.

2.5 OPAL Mission Concept

The OPAL Mission Concept was developed in the Space Systems Design Course at Utah State University, Spring 2012 [26]. The mission plan flies a constellation of 10 sensors in a single orbital plane allowing for measurements with 10 minute revisit time. This

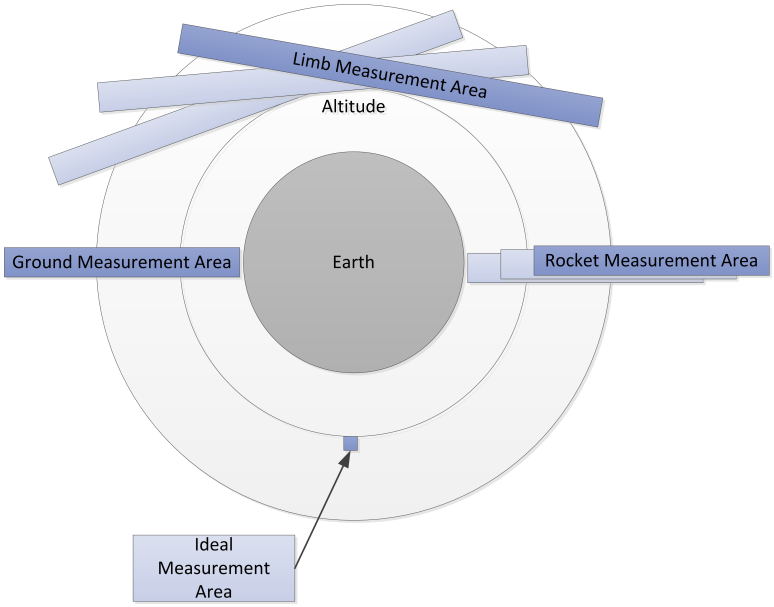

Fig. 2.13: Measurement areas from different platforms.

constellation will provide spatial and temporal resolution never before possible at a cost consistent with NASA Edison or similar programs. OPAL will operate from a 3U CubeSat platform shown in Figure 2.14.

The CubeSat will fly in a lawn dart configuration to minimize drag, with the instrument aperture on the nadir (earth facing) surface. The OPAL sensor will view the limb of the earth behind the satellite along the velocity vector, as shown in Figure 2.15.

Multiple OPAL CubeSats will be deployed from the same launch vehicle. Micro Pulsed Plasma Thrusters (MPPT) by Busek, shown in Figure 2.16, will be used to distribute the individual satellites into repeating ground trace orbits, shown in Figure 2.17. Repeating ground trace orbits result in satellites passing over the same point on the surface of the earth. Since the earth rotates, but satellite orbital planes do not, this means that the orbital plane for each satellite must be rotated based on the time between each satellite pass.

The OPAL sensor generates a large volume of data. The L3 Cadet Radio is capable of handling the large data volume while consuming power levels feasible for a CubeSat. A constellation of up to 10 CubeSats equally spaced around the orbit can share a single

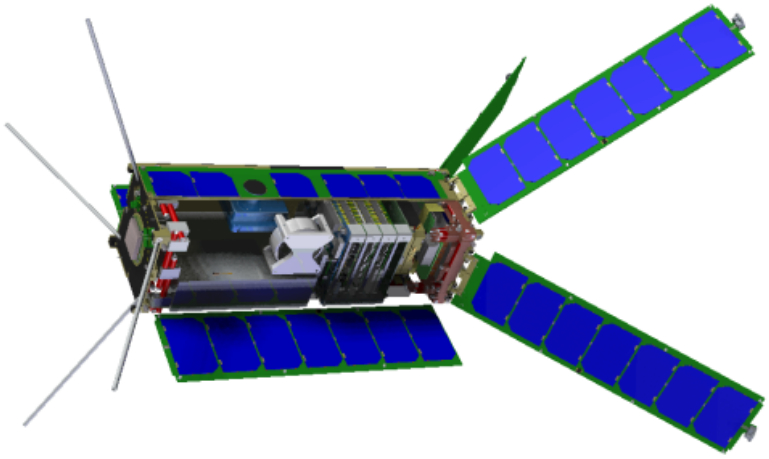

Fig. 2.14: OPAL (grey box in lower left corner) and required supporting equipment in a 3-U CubeSat.

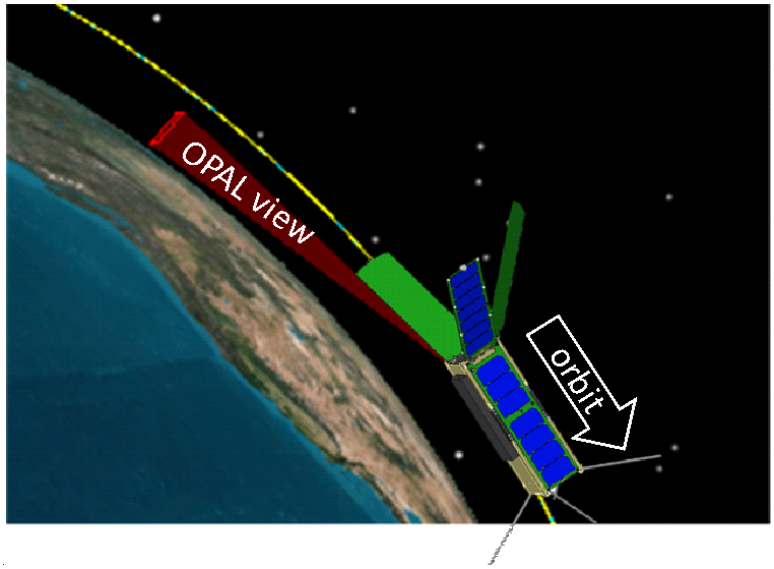

Fig. 2.15: View direction of the OPAL instrument.

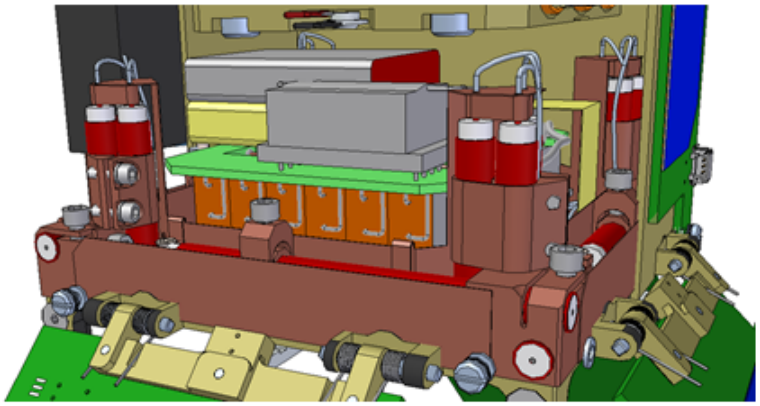

Fig. 2.16: Busek MPPT integrated on a CubeSat. (Image: Busek)

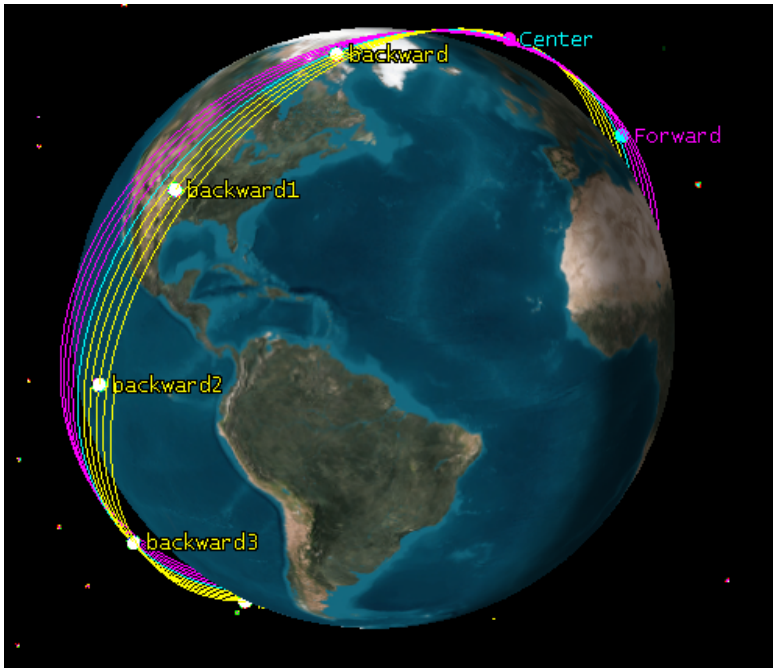

Fig. 2.17: Satellites in repeating ground trace orbits. (Image: Atkins)

dedicated ground station without overlapping communication windows.

The OPAL sensor requires stringent attitude knowledge and control. The knowledge requirement can be met with a single Sinclair star tracker. Attitude control can be provided by the MPPT. Since the MPPT device has minimal flight heritage, a reaction wheel and a set of torque coils will be included as an alternate attitude control system.

The PEARL avionics stack developed at SDL has sufficient processing capability to support the OPAL sensor, power conditioning, the Cadet Radio, and required attitude determination and control hardware.

The OPAL system requires an orbit average power of 11.8W. The most straightforward method of collecting this power is with three fixed and five deployed solar panels. When the satellite flies in a nadir-pointing, lawn-dart configuration in a high inclination orbit, this configuration provides nearly constant orbit average power throughout the seasons. The OPAL instrument, mounted on a 3-U CubeSat with deployed solar panels, radio antennas and light baffle is shown in Figure 2.18.

2.6 SEDI Mission Concept

The SEDI mission concept is identical to the OPAL mission concept described above, but with a SEDI instrument added. The SEDI instrument fits in a 6-U CubeSat with enough room for an OPAL instrument and necessary supporting hardware. Figure 2.19 shows the two instruments in a 6-U volume. The supporting hardware for SEDI and OPAL is the same as described for OPAL alone, but with more powerful attitude control hardware.

Baffles are required to reduce unwanted light. SEDI requires a smaller baffle than OPAL because the entrance aperture is recessed inside the satellite and an internal field stop is capable of rejecting off axis light. Since SEDI observes higher altitudes than OPAL, there are fewer sources of unwanted light. Baffles for both SEDI and OPAL are stowed against the surface of the spacecraft for launch and deploy once on orbit. Notional SEDI baffles are shown in Figure 2.20.

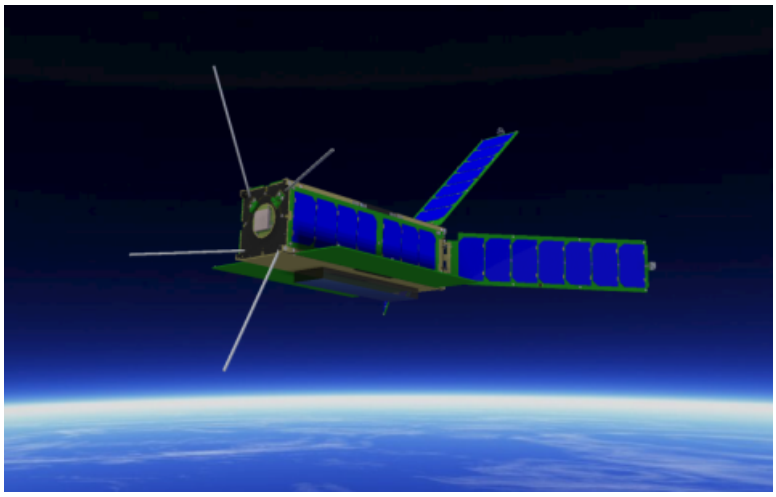

Fig. 2.18: OPAL instrument in flight configuration.

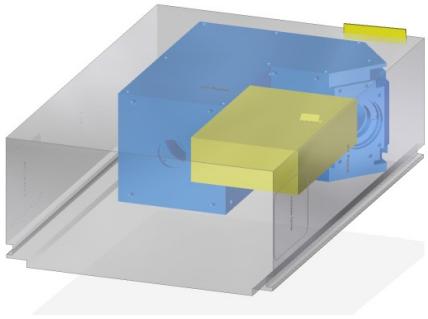

Fig. 2.19: SEDI (blue) and OPAL (yellow) in a 6-U CubeSat.

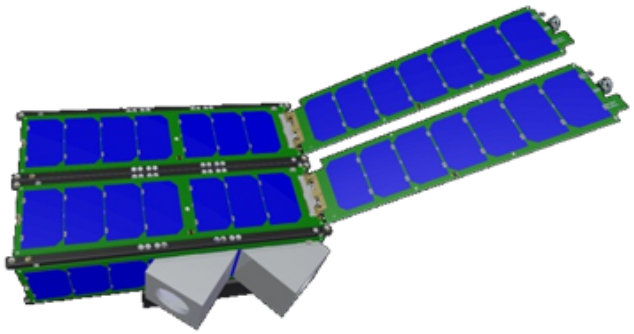

Fig. 2.20: SEDI baffles deployed from a 6-U CubeSat.

Chapter 3

Prototype OPAL

A demonstration prototype of the OPAL sensor was made using commercial off-the-shelf parts to prove the measurement concept in a laboratory setting. The prototype is larger than the flight version because standard size lenses and mounts were used and no fold mirrors were included. The prototype operates with an SDL Digital Imaging Space Camera (DISC) camera, which is one of the options for the flight camera. Since the O2 A-band at 762 nm is absorbed in the atmosphere and is difficult to produce in the laboratory, the prototype was designed to detect a doublet line of mercury. The prototype camera is shown in Figure 3.1.

3.1 Why Mercury?

All of the operational POET sensors must operate around 762 nm to detect the O2 A-band emissions. This wavelength happens to be strongly absorbed by oxygen. The thermosphere is optically thin, which means a photon can be emitted and travel many kilometers to a detector with a small chance of being absorbed by an oxygen molecule along the way. While 762 nm light can be emitted on the surface of the earth, significant absorption will take place between the light source and the detector. This phenomenon complicates the testing of O2 A-band detectors.

One solution to the testing difficulties is to test at a different wavelength. Mercury (Hg) emission spectra has closely spaced peaks near 577 nm, as shown in Figure 3.2, which allows a mercury lamp to qualitatively represent an O2 A-band source [24]. The spacing of both the O2 and Hg line pairs are approximately 2 nm. Since the spacing between the peaks is known, the spectral resolution of the sensor can be determined by measuring the resolution of the two peaks. The resolution should be the same when the system is re-

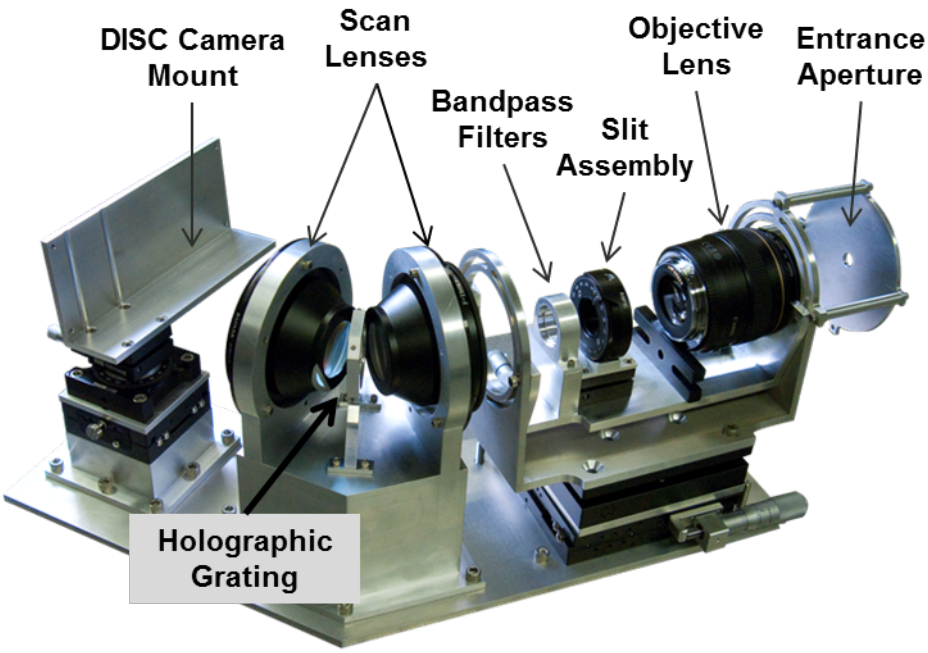

Fig. 3.1: Prototype OPAL. (Image: Jacob Givens)

designed to operate at 762 nm. The mercury wavelength has the additional benefit of being in the visible spectra and therefore compatible with standard off-the-shelf optics. The use of standard optics dramatically lowers the cost for the prototype sensor.

Most mercury calibration sources only contain the Hg-198 isotope of mercury. The spectrum of this isotope is shown above. A spectrum of naturally occurring mercury contains additional peaks in this region. It should be noted that many reference materials only show spectra for naturally occurring mercury.

3.2 Test Stand

3.2.1 Goals

The prototype OPAL sensor is a pathfinder for future operational OPAL sensors. The goal of testing the prototype model was to prove the design concept before producing operational units. While there are differences in form and wavelength, the concept of operations, spatial/spectral resolution, and optical tolerances will remain the same between

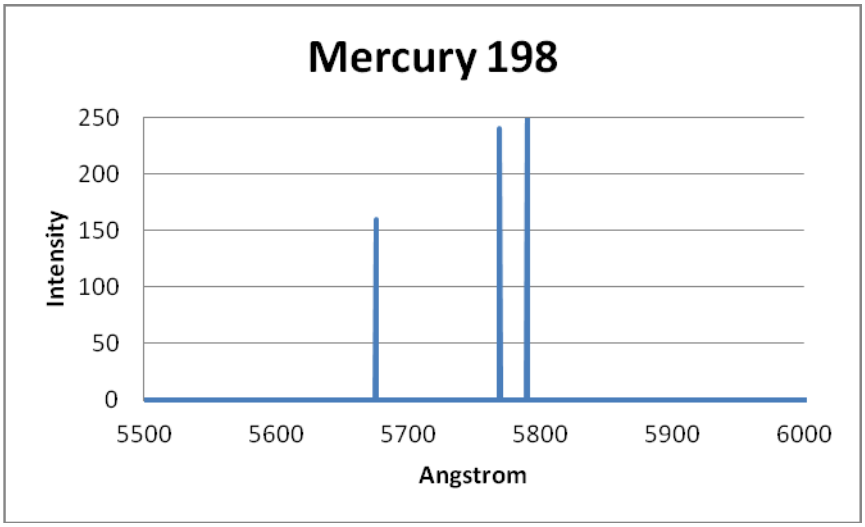

Fig. 3.2: Mercury lamp emission spectra.

the prototype and operational units.

The specific items to be tested were detector response, spectral response, optical throughput, and spatial response.

3.2.2 Procedures

All testing was conducted in the OPAL lab. This room has no windows and few other active experiments, which simplifies the process of creating a completely dark environment. Test equipment was borrowed from SDL and EDL research groups. The test procedure in the Appendix includes is the final testing procedure used for OPAL.

Optics Only Tests

Preliminary tests for optics alignment were performed without a detector. All sensor elements were mounted to the optics table. A Fiber Lite 3100 broadband lamp and a UVP 90-0012-01 Mercury Pen-Ray lamp were used as light sources. A fiber optic light guide was attached to the broadband source to control the location of the source light. The broadband source light was placed at the focus of the OPAL sensor. Filters were removed from the OPAL instrument. This resulted in a rainbow pattern on the detector, shown in Figure 3.3. The width of the rainbow was fixed. The entire rainbow spectra moved up or down with

the point source light, as expected.

For a test of a diffusely illuminated target, the OPAL aperture was covered with white copy paper. The Fiber Lite 3100 source was used to illuminate the back side of the paper. With all the filters in place on OPAL, yellow-green rainbows appeared on the focal plane. Since the filters are too wide for a broadband source, the spectra overlapped making it unreadable. This test was repeated with the mercury light placed in the aperture. Since the mercury source only has peaks in a narrow portion of the spectrum passed by the filters, the resulting spectra did not overlap. Simulated focal plane images are shown in Figure 3.4.

Detector Only Tests

Detector tests were performed without any optics in the train between the light source and the detector. The detector in the OPAL instrument is the Digital Imaging Space Camera (DISC), which has spaceflight heritage.

While performing initial testing on the detector, we realized the camera has a rolling shutter. (One shutter rolls across the image to reset pixels. After the specified integration time, the second shutter rolls across the image to read pixels.) The shutter can operate faster than 60Hz. This is problematic because AC powered lights have intensity fluctuations on a 60Hz cycle. This results in images with stripes, as shown in Figure 3.5. One solution to this problem is to purchase new DC light sources. Unfortunately, some supposed DC light sources, such as the Fiber Lite 3100, have enough residual AC signal to still be problematic. Purely battery powered light sources, such as flashlights, can be successfully used. Another

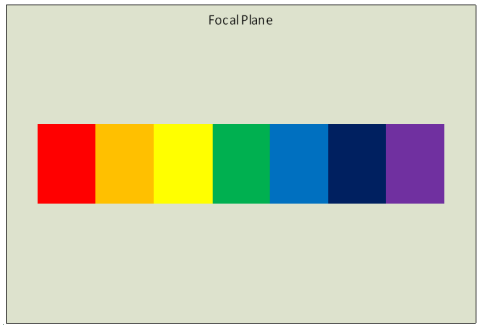

Fig. 3.3: Simulated focal plane image of point source, no filters.

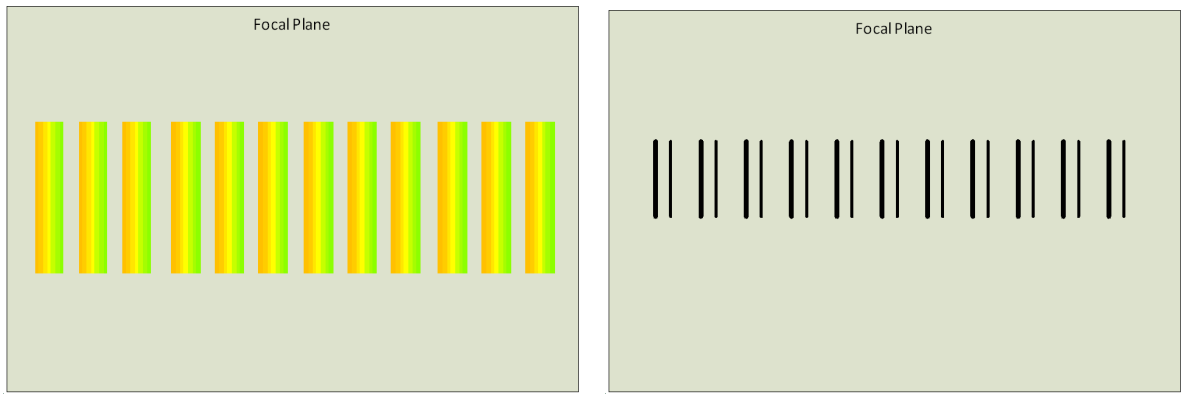

Fig. 3.4: Image of diffuse mercury lamp, with filters, left is as seen by the naked eye, right is as seen by the detector. The human eye is not able to resolve the two lines for each slit because the physical spacing is very small.

solution is to select integration times that are an integer multiple of the period of a 60Hz light (16.6 ms). An integration time of 66.6 milliseconds is exactly 4 cycles of a 60Hz period. When the integration time is set to this integer multiple, the horizontal stripes in the image disappear, as shown in Figure 3.6.

Figure 3.6 plots average pixel intensity along a column to give a line representation of the image. (Imagine squishing Figure 3.5 into a single horizontal line of bright and dark pixels. Plot intensity of each pixel on the y-axis and the position on the horizontal line in the x-axis.) When integration times are an integer multiple of 16.6 ms, the intensity line is smooth. The gradual curvature to the lines is due to uneven target illumination.

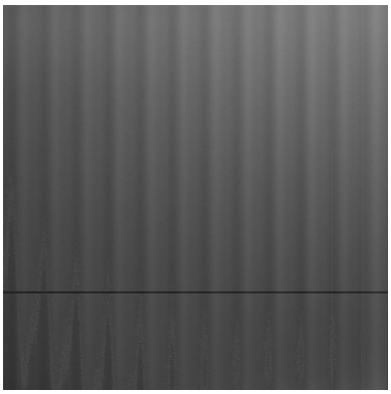

Fig. 3.5: Vertical stripes due to rolling shutter interaction with AC lights. Horizontal line due to detector damage.

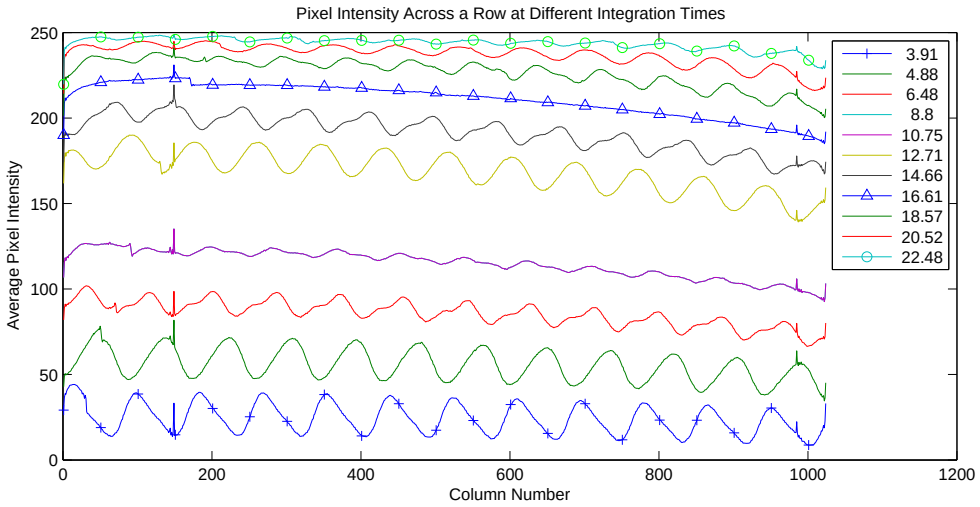

Fig. 3.6: Pixel intensity across a row for different integration times. For integration times that are integer multiples of 60Hz, the fluctuations disappear.

Dark images were obtained by placing the camera in a dark box in a dark room. The edges of the dark box are sealed with black fabric, as shown in Figure 3.7. Images were taken with an integration time of 6403 ms, the maximum allowed by the lab software. Images taken in sequential order had increasing dark current, shown in Figure 3.8, which prompted the author to conduct additional tests. It was quickly discovered that the camera was heating up, as indicated by an internal temperature sensor, and increasing the dark current. The cause of the heating is a hardware malfunction. Since future OPAL instruments will use a different focal plane, troubleshooting of the camera electronics was not performed.

To compensate for the heating of the focal plane, all tests were conducted after the camera was given 3-4 hours to stabilize at a high temperature. Noise caused by temperature is high, but fairly constant. After the camera stabilized, dark images were collected for many integration times. In Figure 3.9, each data point is the average across 10 images at the specified integration time. Noise in dark images was found to be nonlinear for low values of integration time. This phenomenon is likely caused by the low voltage reference of the ADC in the camera set too high. When the signal level is of a magnitude similar to the error in the low voltage reference, there is significant error in the ADC output. Once the reading is significantly greater than the error in the low voltage reference, the induced

Fig. 3.7: Dark box setup.

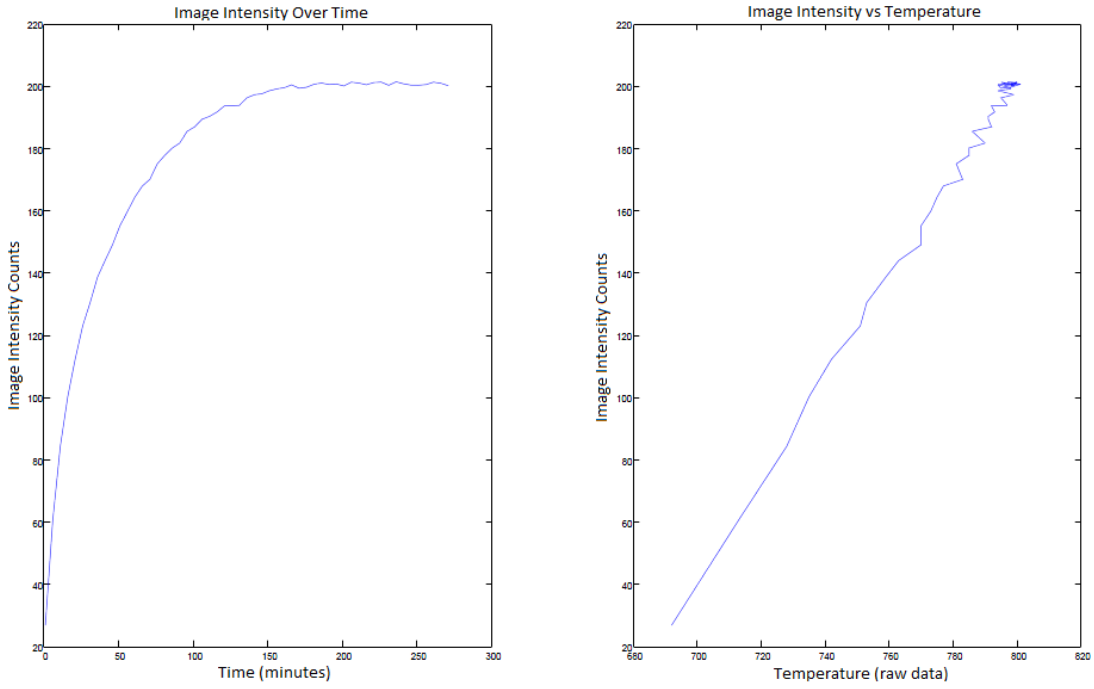

Fig. 3.8: Left: Dark noise increasing then stabilizing with time. Camera was powered on at time = 0, after which it heats up. Right: Correlation between temperature and dark counts. An unknown hardware issue causes the focal plane to heat up over time.

error is trivial.

Extensive data sets were collected to determine the gain and dark current of the detector, with 45 images collected for each set. Three tests were performed: short exposure, no light; short exposure with light; and long exposure with no light. The short exposure time was set so there was detectable dark noise in most pixels within the image (approximately 2 seconds). The long exposure time was the maximum time allowed by the detector software (approximately 6 seconds). The light source was a battery powered flashlight placed at the other side of the lab to create a small point source, as far away as possible. This would result in nearly uniform irradiance across the focal plane. A paper diffuser was placed in front of the flashlight. The opacity of the diffuser (number of sheets of tissue paper stacked together) was selected such that the detector was approximately half way saturated at the pre-selected short integration time. The data from this collection was used to create a Gain Map and a Dark Current Map using the Noise_Study Matlab scripts written by the author. Sample maps are shown in Figure 3.10.

Full System Tests

When the DISC imager is mounted in the OPAL instrument, it is mounted at a 90 degree angle. All images in this thesis have been rotated to display correctly.

Spectral Resolution: Spectral resolution was determined by processing images of a mercury lamp. The images were collected using the configuration shown in Figure 3.11. The mercury lamp was placed a few inches from the input aperture. A glass diffuser caused uniform illumination across the aperture. OPAL was inside a cardboard box to prevent light from entering the instrument at locations other than the input aperture. The mercury lamp was placed in front of the diffuser.

The resulting image from the above test setup is shown in Figure 3.12 (top). Figure 3.12 (bottom) is a linear representation of the intensity of pixels along a row in the image. The wavelength spacing between peaks is known to be 2.1065 nm [24]. The spacing between the peaks on the focal plane is measured at 22.5 pixels, which results in a dispersion of 0.0936

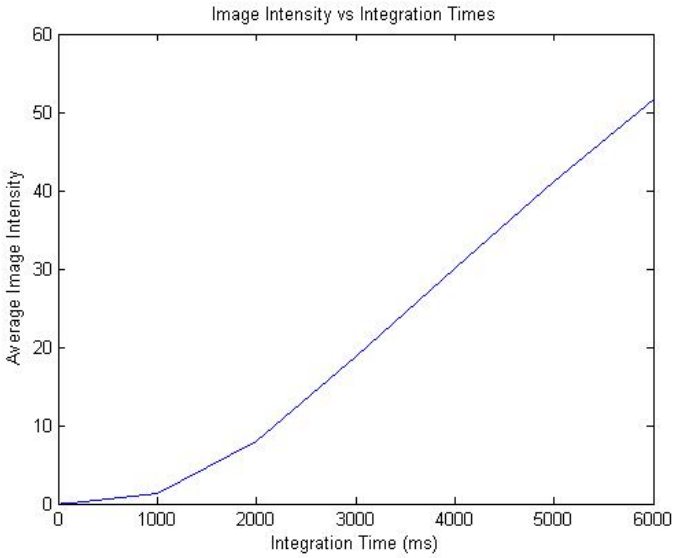

Fig. 3.9: Image intensity vs integration times for dark images. Test performed with cold camera.

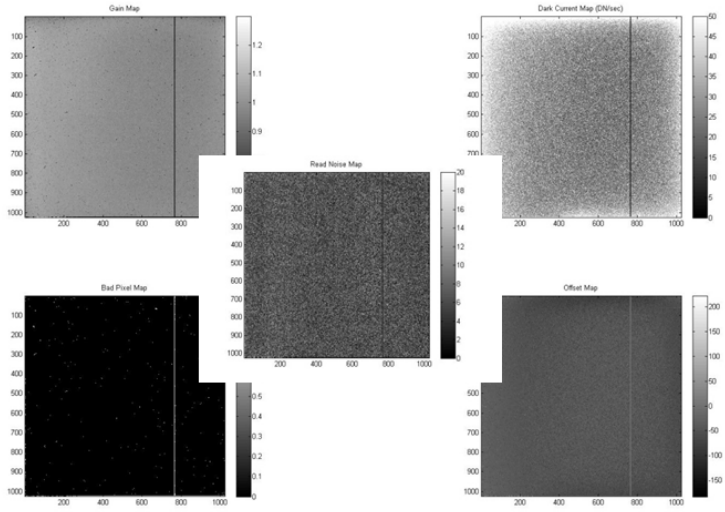

Fig. 3.10: Calibration images: gain, dark current, bad pixel, offset, and read noise.

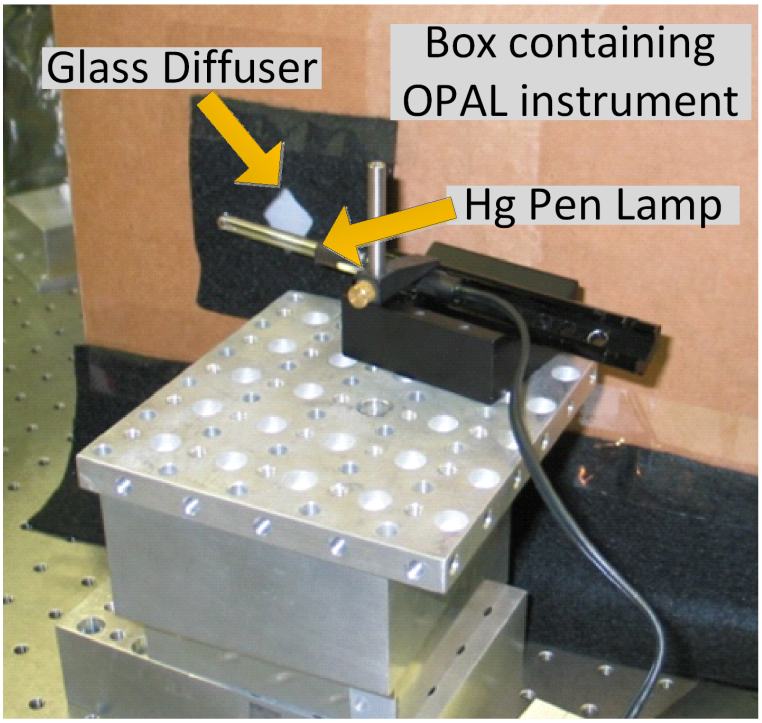

Fig. 3.11: Diffuse mercury illumination setup.

nm/pixel. The inverse of this is that the focal plane has 10.7 pixels per nm wavelength of light. The average full width half maximum (FWHM) of the peaks varies with intensity. For a low intensity mercury lamp, the average FWHM of a single line in the OPAL image is approximately 2.7 pixels. The 577 line was observed to have a slightly wider FWHM than the 579 line. Based on these calculations, the OPAL instrument should be able to resolve peaks with spacing greater than 0.25 nm. A summary of OPAL's spectral performance is shown in Table 3.1.

Table 3.1: OPAL prototype spectral performance.

Light spread across a pixel	0.0936 nm of light/ pixel
Pixel per nm of light	10.7 pixels/ nm of light
Full Width Half Max of peaks	2.7 pixels
Spectral Resolution	0.25 nm

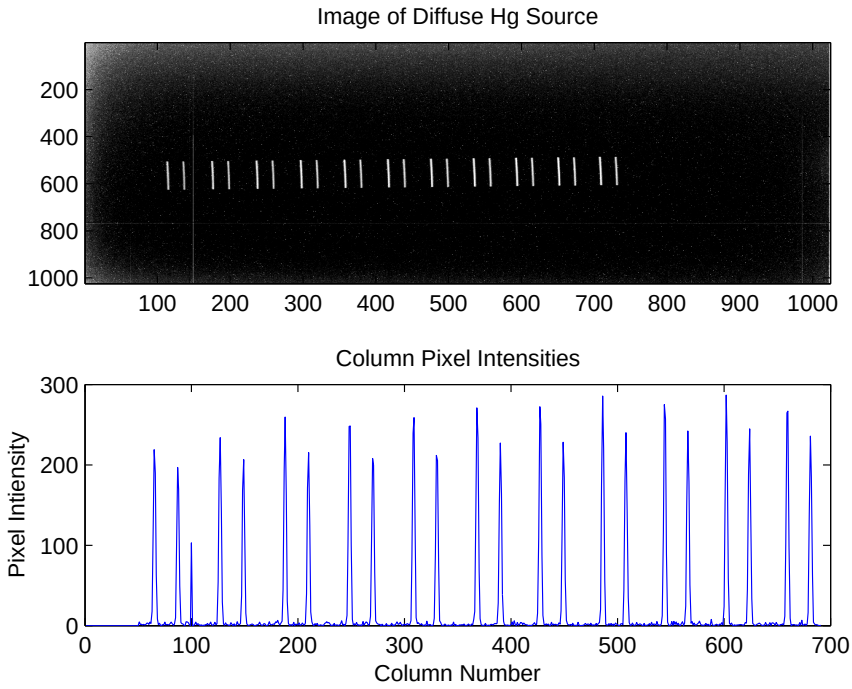

Fig. 3.12: Top: OPAL instrument image of diffuse mercury lamp source. Vertical dimension is true vertical data, horizontal dimension is spectral data. The prototype OPAL instrument has 11 slits, thus showing 11 line pairs in the vertical direction. Bottom: Profile of the intensity along the horizontal axis.

Field-of-View: The field-of-view of the instrument was determined by moving targets in front of the instrument and recording locations where the targets were detected. Targets were made by printing a single white stripe surrounded by solid black on a sheet of paper. The white line target was moved across the field-of-view of the camera while collecting image data, as shown in Figure 3.13. From this data, the FOV was determined to be 1.0 degrees (17 mrad) in height and 4.9 degrees (86 mrad) in width. For a target placed 1.0 m from the aperture, this translates to 1.75 cm height by 8.5 cm width.

Spatial Resolution Test: The OPAL imager has fine spatial resolution in the vertical direction. In the horizontal direction, only a single line for each slit is resolved, which results in very coarse resolution. A vertical spatial resolution test was conducted with black and white striped targets, as shown in Figure 3.14. Targets were printed with a laser printer and mounted to card stock for support. Targets were made with line pair widths ranging from 1 mm to 6 mm. (A line pair consists of one black line and one white line.) The line pair size of the smallest target was limited by the capabilities of the office printer. The width of the targets was 8 inches to ensure the horizontal field-of-view was overfilled. A black background was mounted to the wall in front of the OPAL imager. The distance from the aperture to the wall was 1.76 meters. Targets were taped to the background with double stick tape. Images were collected of each target. The target was illuminated with a broadband source. The slit array was in place for these tests.

Data from the spatial resolution test was processed in Matlab. The modulation transfer function (MTF) is a standard measure of image resolution. The MTF is computed independently for each column of an image and averaged across columns for the overall MTF. The MTF of a single column is the difference of the maximum and minimum intensities divided by the sum of the maximum and minimum intensities.

$$MTF = \frac{(max - min)}{(max + min)}$$

Alternatively, for a sine wave,

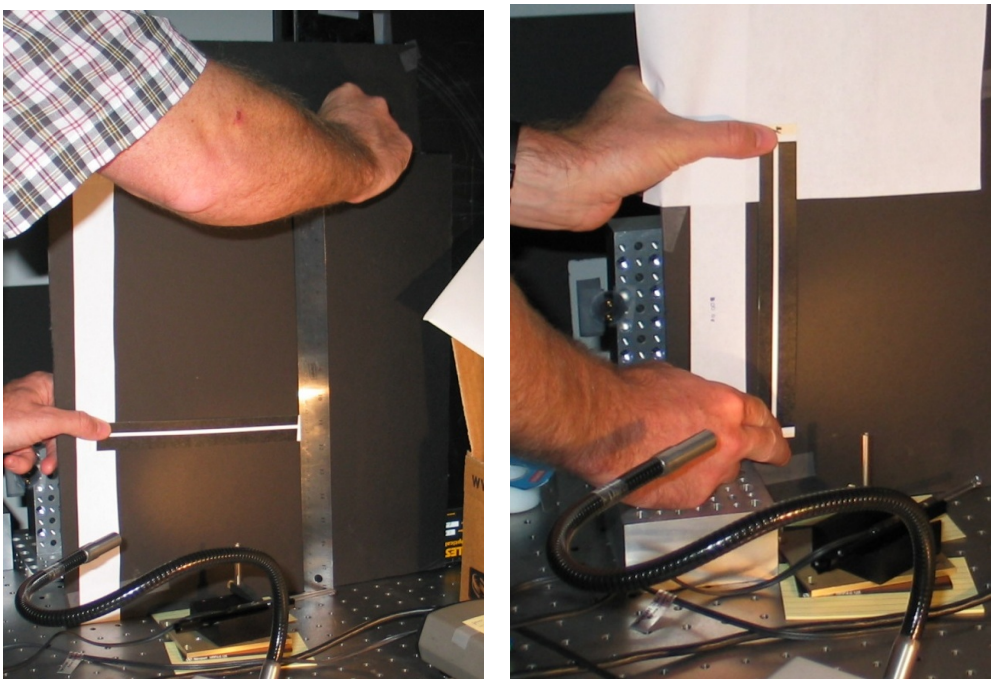

Fig. 3.13: Field-of-view target placement.

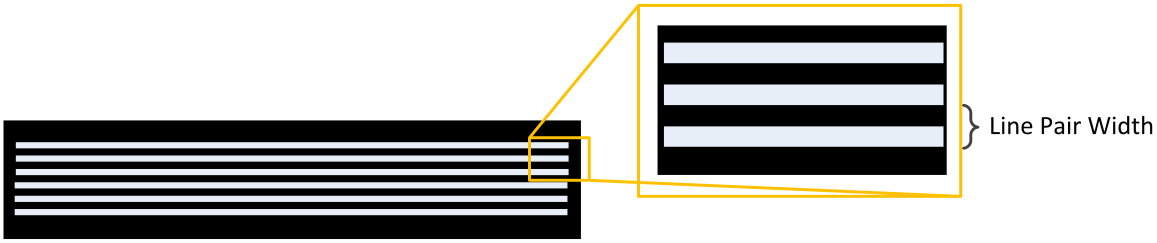

Fig. 3.14: Resolution target. A line pair is one black line and one white line.

$$MTF\,of\,a\,sine\,wave\,=\,\frac{amplitude}{mean},$$

where mean is the DC offset of the sine wave. To determine the maximum and minimum intensities, the intensities along each column were individually fitted to a sine wave in Matlab. Selected line fits are shown in Figure 3.15.

The amplitude of the sine wave was divided by the DC offset (mean) to determine the MTF of a single row in the image. The MTF was averaged across columns to obtain the MTF of the image. Figure 3.16 shows the linear relationship between the MTF of an image and the number of line pairs per degree. Line pairs per degree is used rather than target size to account for distance from the camera to the target.

For this study, resolution was defined as MTF greater than 0.3. Using the chart above, MTF of 0.3 translates to 23 line pairs per degree or 0.045 degrees (0.79 mrad) vertical resolution.

Radiometric Intensity: Radiometric intensity was measured by placing a target of known intensity in the field-of-view of the camera. The test setup is shown in Figure 3.17. Camera read out was compared with predicted intensity levels.

A target of known intensity was created by placing the mercury lamp near the bottom of a sheet of white paper. An opaque block was placed between the lamp and the OPAL aperture to prevent imaging of the lamp bulb. The light from the bulb reflected off the white paper to create a target. The placement of the lamp was a balance between uniform illumination and intense illumination. The final lamp placement was based on a visual assessment of an acceptable level of uniformity. The illumination received on target was measured with a handheld optical power meter. The filters from the OPAL instrument were placed over the power meter to ensure that the meter was detecting the same wavelengths that would be passed through the instrument. The measured radiance on target compared

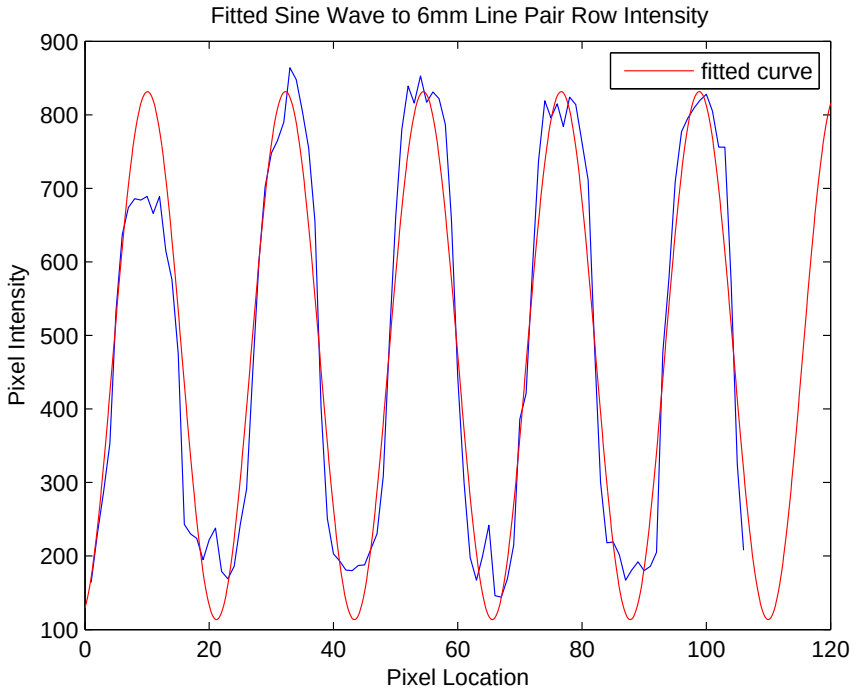

Fig. 3.15: Sine wave (red) fitted to image intensity data (blue) for one column of a 6 mm line pair image.

well with predictions. An attempt was made to detect the irradiance level at the FPA location within the OPAL instrument, but the meter was not sensitive enough for an accurate measurement.

A radiometric budget for the prototype OPAL model was created in Excel. This model incorporates the target illumination, how the light passes through the instrument optics and the detector performance. Detector and optics performance parameters measured in the lab were used, if available. Parameters that were not measured were obtained from manufacturer data sheets or were estimated. The results from actual lab tests were compared with the model. The model results showed the correct general trend, but require additional research for quantitative accuracy. Primary error sources were from the non-uniformities in illumination, difficulty in measuring source intensity and excessive noise from the detector unit that was available at the time of testing.

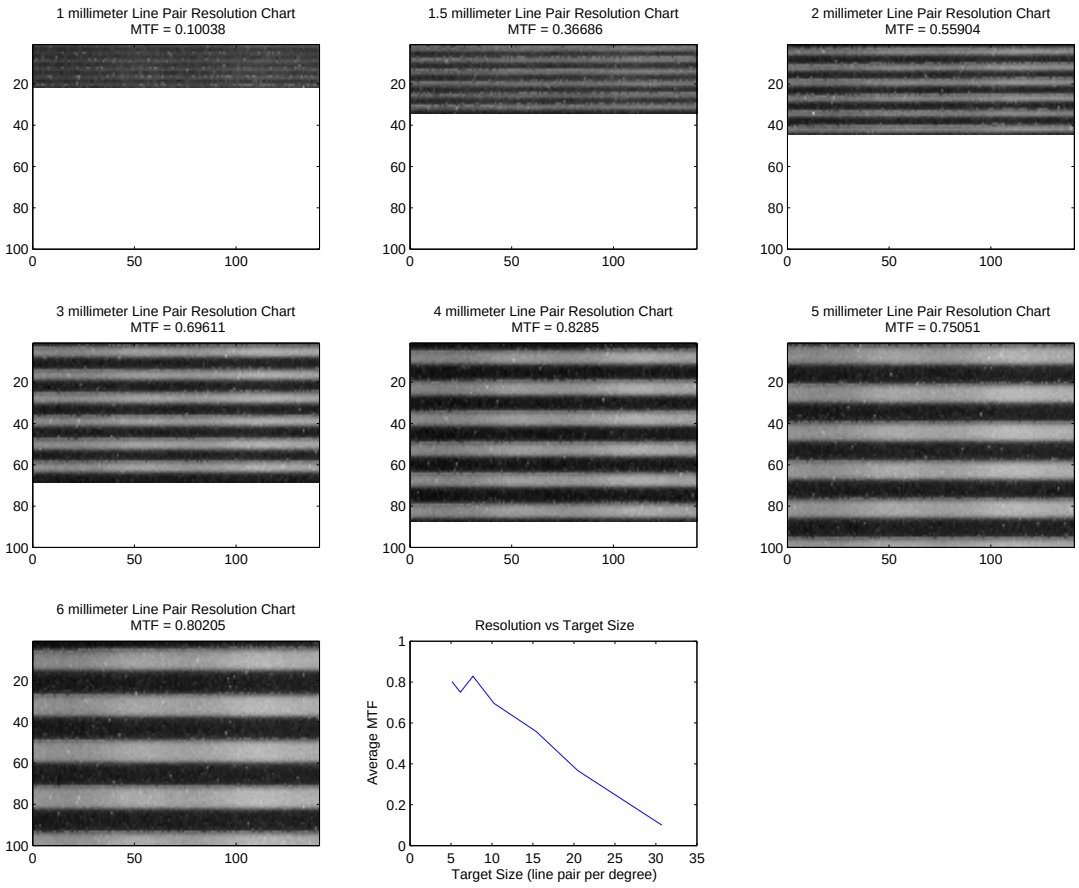

Fig. 3.16: Images of seven targets and the associated MTF.

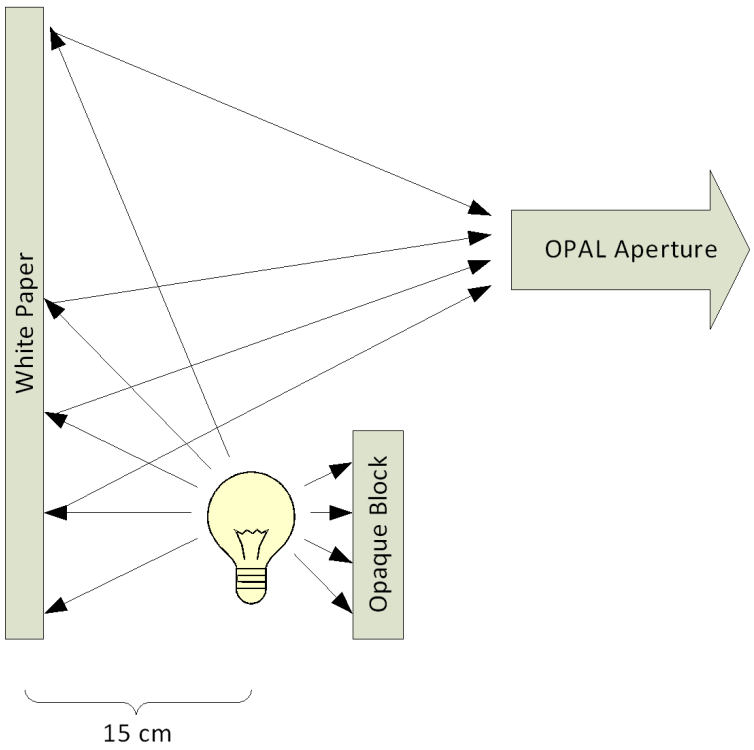

Fig. 3.17: Radiometric test setup. Mercury pencil lamp emits light rays in all directions. Rays scatter off the diffuse white paper and a small fraction enter the OPAL aperture. An opaque block prevents OPAL from viewing the source lamp directly.

3.3 Test Results

The purpose of the prototype OPAL testing was to determine if the flight model OPAL is likely to perform as required. The performance requirements of interest to this study are ability to detect low-light levels and spectral and spatial resolution. The primary differences between the prototype and flight models are the wavelength, size and focal plane.

3.3.1 Radiometric Throughput

Radiometric assessment was attempted, but only poor results were obtained. The data that was collected suggests that the system will work as expected, but did not quantifiably prove this claim. The poor radiometric data is due to the detector used. The new Has-2 focal plane with fully-functional electronics and thermoelectric cooling will be used in all follow-on instruments.

3.3.2 Spectral Resolution

The spectral resolution required for the OPAL instrument is based on the temperature dependent change in the O2 A band emission spectra. The flight unit is required to have a precision of 4 degrees K at an elevation of 100 km. This requires a resolution of <0.6 nm [25].

The prototype OPAL has a spectral resolution of 0.25 nm. For this assessment, resolution is defined as:

$$\begin{aligned} \textit{resolution} \quad &= \quad \textit{spectrometer dispersion across each pixel *} \\ &\quad\quad\;\; \textit{FWHM of peak from monochromatic input.} \end{aligned}$$

A spectral resolution of 0.25 nm is more than sufficient to determine a 4 degree K temperature change. For comparison, RAIDS had a spectral resolution of 0.84 nm [27] and OSIRIS has a spectral width of 0.4 nm [4].

The differences between prototype and flight models will affect the spectral resolution. The wavelength of the flight unit is 32% longer (762 nm vs 577 nm). The longer wavelength will have greater dispersion, which will decrease spectral resolution. The change in detector

will also decrease resolution because the pixel pitch is 20% larger (18 μm vs 15 μm); however, since the system is not pixel limited this will have a minimal effect. The flight detector is expected to have much lower noise than the prototype detector, which will improve the signal to noise ratio. Since the most significant parameter in determining spectral resolution is slit width, which will remain the same between prototype and flight models, the expected change in spectral resolution is small.

3.3.3 Spatial Resolution

The spatial resolution requirements for the flight OPAL are not very demanding. The vertical resolution requirement is a resolved 0.13 degrees. The horizontal resolution requirement is 3.32 degrees. This is sufficient for 5 km vertical and 125 km horizontal resolution from a notional low earth orbit. The field-of-view requirement is 1.06 degrees in the vertical dimension and 13.04 degrees in the horizontal dimension. This corresponds to a FOV of 40 km by 500 km (modified from [25]). The spatial resolution tests demonstrated performance well below the maximum allowed, as shown in Table 3.2. The field-of-view tests showed performance slightly out of specifications, but this will be corrected for the flight model.

The differences between the prototype and flight models will have minimal effect on spatial and spectral resolution, besides changes to increase the FOV. Since the optics are designed for visible to near infrared, the differences in wavelength between the prototype and flight models should have little to no effect on spatial resolution. Spatial resolution is primarily determined by the slit spacing in the horizontal dimension and f# in the vertical dimension. The slit array dimensions will remain approximately the same while the focal

Table 3.2: OPAL spatial resolution and field-of-view.

Resolution (max)		**Required**				**Prototype**	
	Vertical	5	km	0.13	degrees	0.045	degrees
	Horizontal	125	km	3.32	degrees	0.44	degrees
FOV (min)							
	Vertical	40	km	1.06	degrees	1.0	degrees
	Horizontal	500	km	13.04	degrees	4.9	degrees

length is halved, thus doubling the FOV and horizontal IFOV. This change will cause the flight model to exceed minimum requirements for horizontal FOV. The f# in the custom OPAL optics will remain approximately the same, supporting the same vertical resolution.

3.3.4 Testing Conclusion

The testing and calibration of the prototype OPAL went very well. Some tests had to be modified slightly from initial plans, but for the most part, everything went smoothly. Most issues encountered were due to problems with the focal plane electronics, which will not be used in follow-on OPAL instruments. Radiometric calibration studies produced only very coarse data. The data supports the claim that OPAL will have appropriate radiometric sensitivity, but more work could be done in this area. All test results support the claim that the flight OPAL, with noted modifications, should meet mission requirements.

Chapter 4

OPAL Data Processing

The OPAL instrument generates large volumes of data because it images continuously. Existing data processing techniques to reduce the imagery to temperature profiles are too computationally intensive to be performed on a CubeSat. Currently, there is only one CubeSat radio capable of downlinking the entire OPAL data set, and this radio is not ideal. New on-board processing algorithms are necessary to allow for constellations of OPAL CubeSats.

4.1 Data Processing Theory

The temperature dependent spectra of oxygen are well understood and discussed in Section 1.1.1. Both RAIDS and OSIRIS have used this principle to determine temperature in the lower thermosphere.

The RAIDS experiment had the luxury of a large data downlink capability (by CubeSat standards). Data was downlinked and processed on the ground. Dr. Andy Christensen created a model of oxygen and nitrogen emissions in the thermosphere based on work by Herzberg for the RAIDS program. The resolution of the model is approximately 0.2 nm. The model output was convolved with the expected response of the RAIDS instrument. After correcting for a number of known issues, a least squares fit was performed between the model and observed data. Known issues include glints of ISS structures, and at high temperatures, nitrogen emissions.

4.2 Simplified Data Processing

Least squares fits of hundreds of curves are too computationally intensive to be performed on a CubeSat processor. A computationally simple processing algorithm was devel-

oped with model data. The simplified algorithm performs similarly to the RAIDS algorithms when used on data captured by RAIDS. For this study, the raw RAIDS data was used with the RAIDS predicted temperatures as truth values. This is not an ideal approach to algorithm validation, but very little spectral and temperature data of the thermosphere has been collected.

The simple algorithm is based on bands of interest. Initial bands were selected based on the wavelengths with the most temperature dependent variation. Bands were tuned to get performance similar to the RAIDS processing algorithm and are shown in Figure 4.1. Band locations are typically fixed, but can be adjusted on the basis of on orbit calibration results. A background band was identified adjacent to the A-band to determine light intensity not caused by oxygen emissions. The intensity across each band is summed, allowing the entire spectra to be quickly compressed to integers, which can easily be sent to the ground for further processing. For each image from the flight version of the instrument, there are nine slits, with 15 vertical steps, each represented by four integers. Using this simplified algorithm, a 1Mpixel image is reduced to 540, 32-bit integers. One image every 20 seconds results in an orbit average data production of less than 1kbps, which is reasonable for a CubeSat.

Once on the ground, the normalized background is subtracted from the other bands. The ratio of bands 1:3 and 3:4 are taken. (Band 2 was found not to be necessary.) As shown in Figure 4.2, each ratio correlates to a unique temperature. Either line on the plot in Figure 4.2 can be used to determine temperature.

The simplified algorithm works perfectly against model data. When run against raw data collected by the RAIDS satellite, the simplified algorithm performs similarly to the complex RAIDS algorithm. Figure 4.3 shows the RAIDS prediction against the simplified algorithm prediction. The blue and green markers are the results predicted by a single ratio. The average temperature prediction from each of the two ratios is shown in red. The red markers have a strong correlation to the official RAIDS prediction. Shown for reference, the blue line is a perfect correlation between the two methods.

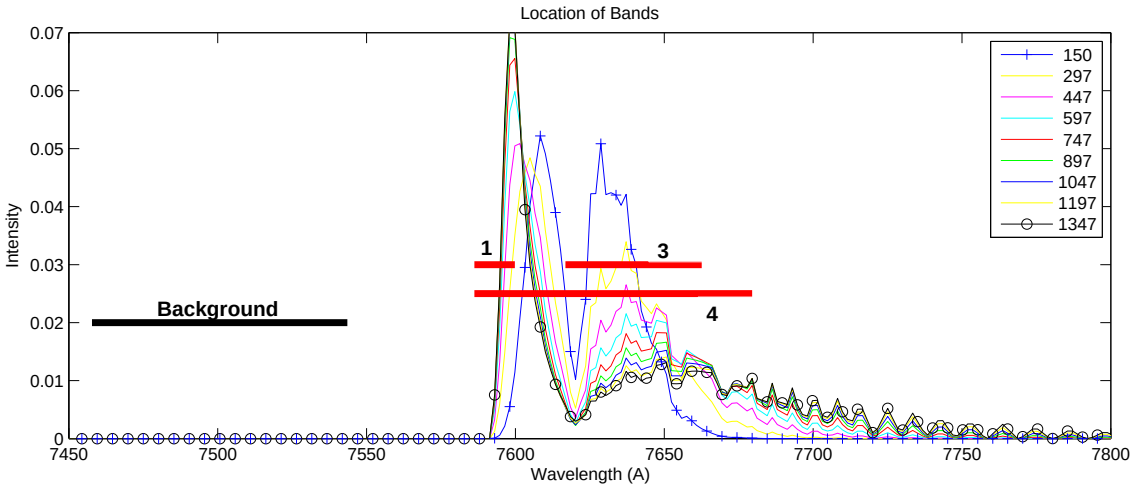

Fig. 4.1: Location of wavelength bands used for simplified processing method.

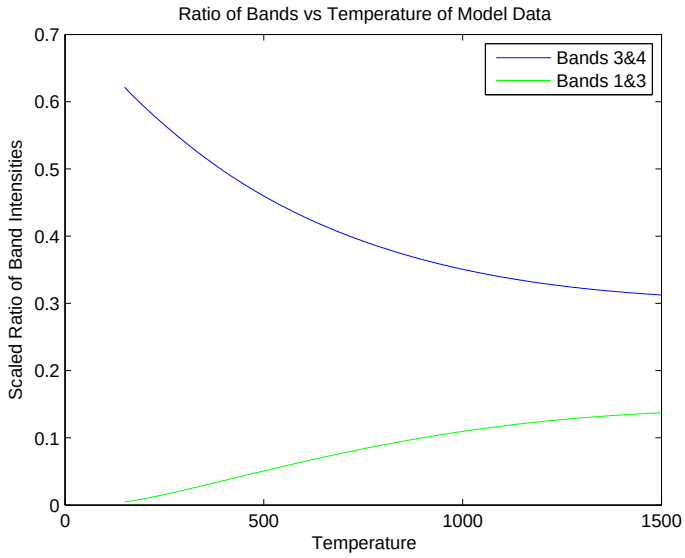

Fig. 4.2: Either the 1:3 ratio or the 3:4 ratio can be used to uniquely determine temperatures.

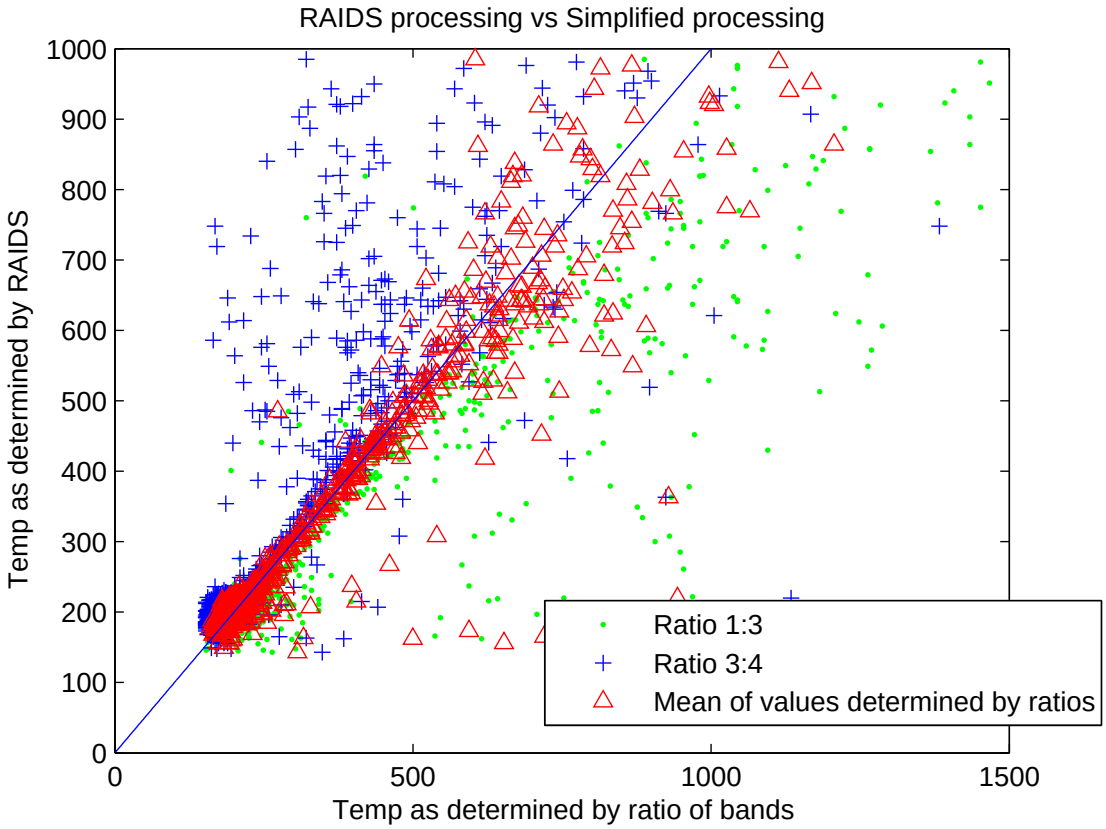

Fig. 4.3: Temperatures as determined by RAIDS processing vs Temperatures as determined by simplified processing. Green dots use only the 1:3 ratio. Blue plus signs use only the 3:4 ratio. Red triangles are the mean of the results from the ratios. Red triangles show the best correlation to the RAIDS results.

The difference between the predications of the simplified method and the RAIDS method (shown in Figure 4.4 blue markers) grows with temperature. The difference between the two methods is similar to the uncertainty in the RAIDS data (Figure 4.4 red markers). Both the difference and the uncertainty are shown as absolute values. There is little correlation between RAIDS uncertainty and the difference between the two processing methods of the same data set. A trend is only apparent when temperature is considered. This may be due to the methods the RAIDS team used to quantify uncertainty.

Errors and uncertainties are greater at higher temperatures. This is expected because higher temperatures occur at higher altitudes where the atmosphere is thinner. When the atmosphere is thin, the detectable signal is low. The noise of the sensor is relatively constant, thus the signal-to- noise ratio at high temperatures is bad.

The differences between the RAIDS predictions and the simplified prediction are similar to the uncertainty in the RAIDS data. Without better truth data, the simplified algorithm cannot be improved. Future research should test the simplified algorithm against ODIN and UARS data.

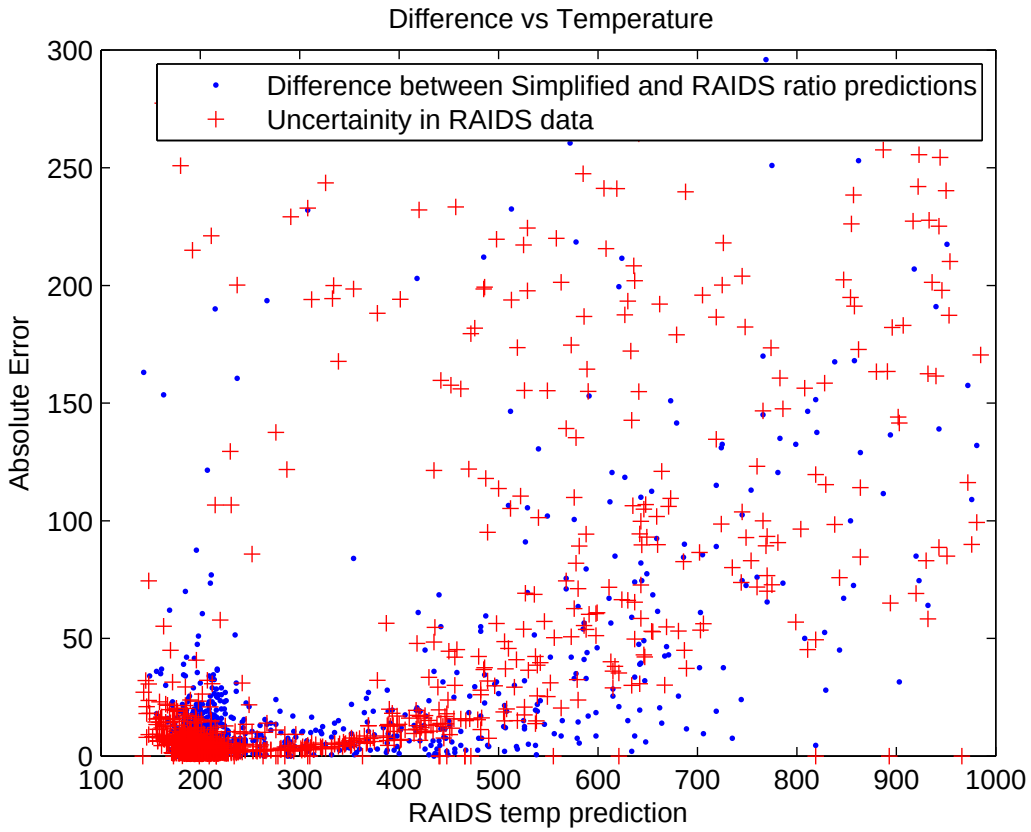

Fig. 4.4: Blue dots: Difference between RAIDS and simplified methods. Red plus signs: Uncertainity in RAIDS data.

Chapter 5

Prototype SEDI

The prototype SEDI sensor is very similar to the flight version of the sensor. This was possible because many of the necessary optics are commercial-off-the-shelf (COTS) parts. The only custom optics are the Fabry-Perot filter and a collimator lens. The custom Fabry-Perot filter was purchased for the prototype unit because there is no acceptable COTS substitute. The custom collimator lens was replaced with a COTS lens for the prototype, which will slightly reduce the resolution of the interferogram. The focal distance on the prototype is adjustable to allow for close targets in the lab while the flight model focal distance is fixed at infinity. Bandpass filters are not included in the prototype because undesired light sources can be excluded from the laboratory and the custom flight filters are expensive. A mode-stabilized HeNe laser will be used as a calibration source rather than a neon lamp due to the missing bandpass filters. The flight detector was replaced with a standard lab camera due to cost.

SEDI detects the Doppler shift of the 630.0 nm oxygen line. The shifts detected are on the order of tens of picometers. Generating known shifts of this magnitude in the lab is difficult. Initial test ideas required moving a 630 nm source towards the SEDI sensor and observing the actual Doppler Effect. Unfortunately the wind speeds in the thermosphere are tens to hundreds of miles per hour, which is not feasible in a laboratory environment.

While moving an object at high speeds in a small lab is not feasible, a disk can be spun at high speeds. The disk must be angled with respect to the detector such that one edge is moving towards the camera and the other edge moving away. Part of the disk face must be visible, so a 60 degree angle between the camera boresight and the disk normal was selected. This setup is shown in Figure 5.1. Under these conditions, a 15 cm disk at 30 revolutions per second can produce a speed differential of 24 m/s between the top and

bottom of the disk. The disk will be illuminated by a mode-stabilized HeNe laser because it has a wavelength of 632.8 nm, which is similar to the 630.0 nm oxygen line. Since the laser light is reflected off the disk, its Doppler shift will be twice that of a molecule passively emitting. SEDI is designed to have a wind speed resolution of <10m/s, which should be observable with the spinning disk setup.

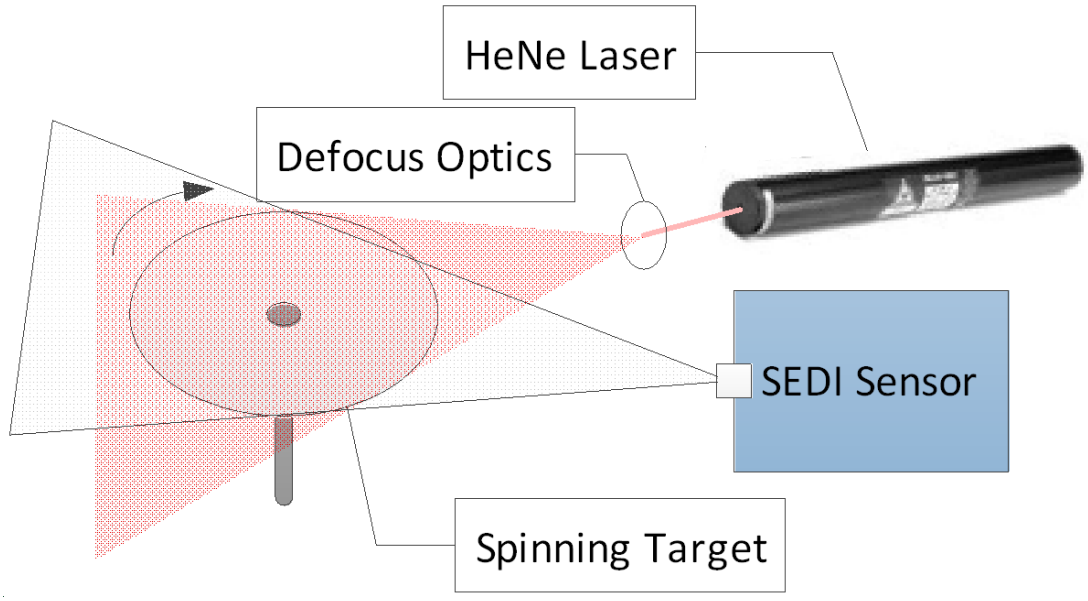

Fig. 5.1: SEDI lab test setup.

Chapter 6

Conclusion

The OPAL temperature sensor and SEDI wind sensor are significantly smaller and lower cost than previous space weather sensors. A constellation of these sensors would provide unprecedented spatial coverage and temporal resolution, which could change our understanding of the sun's influence on the thermosphere.

In conjunction with this thesis, two novel sensors have been developed. The author developed and implemented an OPAL test plan and observed outstanding performance results. The author assisted in design of a prototype SEDI and developed an associated test plan. The prototype SEDI will be built and tested in late 2012. Preliminary designs for host spacecrafts have been completed. The author developed a data processing algorithm compatible with the resources available on a CubeSat. The OPAL and SEDI sensors are ready to be included in flight mission proposals.

OPAL and SEDI require additional research to make them ready for flight operations. The host spacecraft design needs to be finalized. A flight-worthy electronics board for the EMCCD detector needs to be developed. Detailed thermal modeling is necessary to verify the current SEDI design. Future research should include detailed radiometric models of both instruments to gain a better understanding of expected signal-to-noise ratios. The expected signal-to-noise ratios should be used in conjunction with existing ODIN, UARS and RAIDS data to predict uncertainties in on-orbit data. Continued collaboration with the science community is necessary to ensure that the final instrument specifications fulfill science requirements at the time of launch.

References

[1] UCAR. (2011) Spark UCAR science education. [Online]. Available: https://spark.ucar.edu/shortcontent/exosphere-overview

[2] D. Blicq. (2012) Atmosphere. [Online]. Available: http://xnet.rrc.mb.ca/davidb/atmosphere.htm

[3] National Earth Science Teachers Association. (2012) Windows to the universe. [Online]. Available: http://www.windows2universe.org/earth/Atmosphere/layers_activity_print.html

[4] P. Sheese, E. Llewellyn, R. Gattinger, A. Bourassa, D. Degenstein, N. Lloyd, and I. McDade, "Temperatures in the upper mesosphere and lower thermosphere from OSIRIS observations of O2A-band emission spectra," *Canadian Journal of Physics*, 2010.

[5] A. Christensen, J.-H. Yee, R. Bishop, S. Budzien, J. Hecht, G. Sivjee, and A. Stephan, "Observations of molecular oxygen atmospheric band emission in the thermosphere using the near infrared spectrometer on the iss/raids experiment," *Journal of Geophysical Research*, 2012.

[6] V. Krassovsky, N. Shefov, and V. Yarin, "Atlas of the airglow spectrum 3000-12400a," *Planet, Space, Science*, pp. 883–915, 1962.

[7] A. Christensen, 2012, Private Communication.

[8] G. Shepherd, G. Thuillier, W. Gault, B. Solheim, C. Hersom, J. Alunni, J. Brun, S. Brune, P. Charlot, and L. Cogger, "WINDII, the wind imaging interferometer on the upper atmosphere research satellite," *Journal of Geophysical Research*, 1993.

[9] P. Hays, "The High-Resolution Doppler Imager on the Upper Atmospheric Research Satellite," *Journal of Geophysical Research*, 1993.

[10] University of Michigan. (2012) The High Resolution Doppler Imager. [Online]. Available: http://hrdi.engin.umich.edu/

[11] Bill Webster. (2011) 500-mile footprint for debris. [Online]. Available: http://www.washingtonpost.com/national/health-science/500-mile-footprint-for-debris/2011/09/18/gIQAuUjedK_graphic.html

[12] Canadian Space Agency. (2007) OSIRIS at the forefront of the study of ozone depletion. [Online]. Available: http://www.asc-csa.gc.ca/eng/satellites/osiris.asp

[13] GATS, Inc. (2007) Facts. [Online]. Available: http://saber.gats-inc.com/index.php?action=overview

[14] University of Michigan, TIDI Team. (2008) Data quality and validation. [Online]. Available: http://tidi.engin.umich.edu/html/go?scripts/quality_validation.pl&menu_home-new.html

[15] T. Killeen, "TIMED Doppler Interferometer: Overview and recent results," *Journal of Geophysical Research*, 2006.

[16] NASA. (2012) NASA Image: S129E009592. [Online]. Available: http://www.nasa.gov/mission_pages/station/research/experiments/HREP-RAIDS.html

[17] Pumpkin, Inc. (2012) CubeSat Kit. [Online]. Available: http://www.cubesatkit.com/

[18] C. Swenson, "CuPID proposal," 2011.

[19] S. C. Barden, J. A. Arns, and W. S. Colburn, "Volume-phase holographic gratings and their potential for astronomical applications," in *Optical Astronomical Instrumentation, SPIE Proceedings, vol. 3355*.

[20] Semiconductior Components Industries, LLC, "HAS2 image sensor ON semiconductor data sheet," 2012.

[21] V. Khomich, A. Semenov, and N. Shefov, *Airglow as an Indicator of Upper Atmospheric Structure and Dynamics*. Verlag, Berlin, Heidelberg: Springer, 2008.

[22] C. Englert, "Initial ground-based thermospheric wind measurements using Doppler asymmetric spatial heterodyne spectroscopy (DASH)," *Optical Society of America*, 2010.

[23] A. Marchant, 2012, Private Communication.

[24] CRCnetBase. (2011) Handbook of chemistry and physics. [Online]. Available: http://www.hbcpnetbase.com/

[25] C. Swenson, "STEADE storm time energy dynamics explorers proposal," 2010.

[26] S. Whalen, S. Atkin, B. Chase, S. Marchant, M. Tait, and C. Swenson, "Storm-time heating aeronomy research and exploration (SHARE) mission," 2012.

[27] A. Stephan. (2009) Raids: The remote atmospheric and ionospheric detection system. [Online]. Available: http://www.aero.org/conferences/itmr/pdf/24_Stephan.pdf

Appendix

OPAL Prototype Test Procedure

A.1 Optics Only Tests

1. Assemble all optics except camera and slit assembly.
2. Place white card at the location of the focal plane.
3. Place dark housing around instrument (cardboard box with only necessary holes).
4. Illuminate with Fiber Lite 3100 broadband light source in a point source configuration.
    - Observe rainbow pattern on white card.
5. Add slit assembly.
6. Illuminate with Fiber Lite 3100 light source in a point source configuration.
    - Observe rainbow pattern on white card, colors should be more resolved.
7. Illuminate with 90-0012-01 UVP Pen Ray Mercury Lamp (Hg Lamp) in point source configuration.
    - Observe two lines on white card, one for each spectral line of the lamp.
8. Place opal glass diffuser in front of OPAL aperture.
9. Place Hg lamp in front of diffuser.
    - Observe two lines for each slit.

A.2 Focal Plane Characterization Tests

Dark Response

1. Assemble detector with spectrometer optics.
2. Cover detector with light tight box.
3. Turn off room lights.
4. Take a series of 10 data collections at each of the following integration times:
    - 33ms (integer multiple of period of 60 Hz lights)
    - 50ms
    - 66ms
    - 83ms
    - 100ms
    - 116ms
    - 132ms
    - 1000ms (large time steps)
    - 2000ms
    - 3000ms
    - 4000ms
    - 5000ms
    - 6000ms.
5. Take long duration measurement.
    - Take one image with 6 second exposure every 5 minutes for 5 hours.
6. Evaluate data, characterize any changes in detector response.

Dark Current and Detector Offset

1. Place detector on optics bench without spectrometer optics.
2. Cover detector with light tight box.
3. Turn off room lights and computer monitor.
4. Find shortest exposure time that detects signal in most pixels (approximately 2 seconds).
    - Collect 45 images at short exposure time, all dark conditions.
5. Place a DC light source (battery powered flashlight) as far away from the instrument as possible.
6. Create diffuser with copy paper or tissue paper.
7. Place diffuser immediately in front of the light source and aim at detector.
8. Modify distances or diffuser thickness such that the detector is approximately half way saturated at the exposure time selected in step 4.
    - Collect 45 images at short exposure time, illuminated condition.
9. Cover detector with box or dark cloth. Make room completely dark (including turning off the computer monitor and lights in adjacent rooms).
    - Collect 45 images at the maximum exposure time allowed by the software (approximately 6 seconds) in dark conditions.
10. Process data according to the Noise_Study series of Matlab scripts.

Response Uniformity

1. Use DC flashlight as light source.
2. Place flashlight as far away as possible.

3. Place opal glass diffuser in front of flashlight.

4. Point flashlight at camera.

5. Measure detector response. All pixels should produce same output.

A.3 Full System Tests

Out of Band Test

1. Use Fiber Lite 3100 in point source configuration.

2. Use low-pass filter with cutoff below 550 nm over hole in box.

3. Measure detector response.

4. Repeat with high-pass filter with cut-on above 590 nm.

5. Repeat with same illumination conditions, but no filter.

6. Assuming filters pass 1% of the light between 562-587 nm, filtered images should have 1% of the intensity as the unfiltered image.

Spectral Resolution

1. Use Hg lamp as light source.

2. Place opal glass diffuser in front of OPAL aperture.

3. Measure detector response. Resolution of emission peaks determines spectral resolution. Spacing of peaks determines spectral width of instrument.

Field of View

1. Print a horizontal line on a paper target.

2. Mount single target in front of OPAL.

3. Measure detector response.

4. Move target and repeat until edge of FOV is found.

Spatial Resolution Test

1. Print targets of black and white stripes. Sample target is shown in Figure A.1.

    - 1.0mm line pair width
    - 1.5mm line pair width
    - 2.0mm line pair width
    - 3.0mm line pair width
    - 4.0mm line pair width
    - 5.0mm line pair width
    - 6.0mm line pair width

2. Place targets at a known distance from sensor.

3. Use smaller targets until sensor can do longer distinguish lines.

4. Use modulation transfer function to quantify resolution.

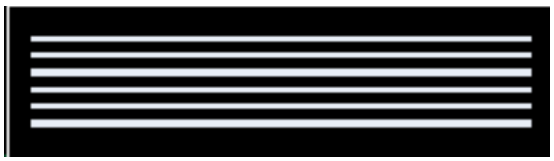

Fig. A.1: Sample resolution target.